To the Graduate Council:

I am submitting herewith a dissertation written by Satya Prasad Mulapudi entitled "Fundamental Studies of X-ray and Secondary Electron Spectroscopy." I have examined the final electronic copy of this dissertation for form and content and recommend that it be accepted in partial fulfillment of the requirements for the degree of Doctor of Philosophy, with a major in Materials Science and Engineering.

David C. Joy

Major Professor

We have read this dissertation
And recommend its acceptance:

Raymond A. Buchanan

Carl J. McHargue

Charlie R. Brooks

Philip D. Rack

Accepted for the Council:

Anne Mayhew

Vice Chancellor and
Dean of Graduate Studies

(Original signatures are on file with official student records.)

Fundamental Studies of X-ray and Secondary Electron Spectroscopy

A Dissertation Presented for the Doctor of Philosophy Degree

The University of Tennessee, Knoxville

Satya Prasad Mulapudi

December 2004

DEDICATION

To my parents Raghava Rao and Sita Maha Laxmi who have supported me all the way since the beginning of my studies.

ACKNOWLEDGEMENTS

I would like to express my sincere appreciation and gratitude to my academic advisor and distinguished scientist, Professor David C. Joy, for his guidance and support throughout the course of this work. His innovative ideas and enthusiasm are inspirational.

I would like to thank my doctoral committee members Dr. R.A. Buchanan, Dr. C. J. McHargue, Dr. C. R. Brooks and Dr. P.D. Rack for their critical appreciation of this work. I acknowledge the help from Dr. Harry Meyer at Oak Ridge National Laboratory.

I am grateful to Dr. A. Eades for giving access to his unpublished study of fluorescent yields, and Dr. M. Procop for valuable discussions and for a copy of his unpublished data on X-ray efficiency. I would like to thank Dr Y. Sakai for permission to use his published data.

I am indebted to my colleagues Xiaohu Tang, Jing He, Dr. Yeong-Uk Ko, Dr. Carolyn Joy, Young Choi, Alexander Thesen, Jihoon Kim, Wei Li, Yinghong Lin and Toshihide Agemura for their sincere help. I deeply appreciate the dedicated help of our group secretary Jennifer Trollinger.

This work was partially supported by SRC under contract LJ-864.003.The contract monitor is Dr. D.Herr. This work was also supported by Oak Ridge National Laboratory which is managed by UT-Batelle, LLC for the U.S. Department of Energy under contract number DE-AC05-00OR22725.

ABSTRACT

Microanalysis of submicron particles in the Scanning Electron Microscope (SEM) is only possible by using low incident electron beam energies due to smaller interaction volume and suppressed beam induced charging. Such low beam energies must use *L*- and *M*-lines rather than the familiar *K*-lines. The information about the fundamental parameters of X-ray emission and transport at low energies is limited, so the use of *L*- and *M*- lines is problematic. The rate of generation of X-rays from an element irradiated at some energy E depends on the product of the ionization cross-section $\sigma(E)$ and the fluorescent yield ω. Unfortunately neither of these quantities is well established independently, especially outside of the *K*-series of lines. Therefore the absolute X-ray generation efficiencies (photons /electron) were directly measured and parameterized for a wide range of *K*, *L*, and *M* lines from different elements. It is anticipated that a complete set of such data would be of great value in applications such as spectrum simulation and standardless analysis.

Secondary electron spectra have been collected from both pure elements and from compounds examined under conditions approximating those found in a scanning electron microscope. Despite the presence of substantial surface contamination these spectra are found to be reproducible and characteristic of the underlying material. Typically the peak in such spectra is found to be at an energy of about 5 eV, and 50% of the total secondary electron emission falls within the range 0-12 eV. These data may be of value for the design of detectors for scanning microscopy and might have applications for microanalysis.

TABLE OF CONTENTS

LIST OF FIGURES

INTRODUCTION

The scanning electron microscope (SEM) has established itself in the semiconductor industry as the most widely used tool for metrology, wafer inspection and defect review. It is estimated that two out of every three SEMs manufactured go to some part or other of the semiconductor industry, accounting for about three out of every four of the dollars spent in this area. However, over the next decade the SEM faces some severe challenges to its position because the continued extrapolation of Moore's law, as quantified by the SIA Roadmap[1], calls for spatial resolution of the order of 1 nanometer (nm) while continuing to operate under conditions designed to maximize the throughput rate. The quest for higher spatial resolution is also of importance in the microanalytical applications of the SEM. As the size of devices is reduced the size of defects that are important is also reduced. There is thus a requirement for the microanalysis of particles, which may now be less than 0.5 μm in size, within a few years may be 0.1μm. Because of the finite size of the beam interaction volume, an unambiguous analysis of such a small volume free from the effects of the substrate is only possible by reducing the energy of the incident beam to a suitably low value.

A significant fraction of all scanning electron micrographs are now taken at beam energies of 5 keV or below and, because many SEMs will mostly be operated in this low-voltage regime, there is thus a growing interest in performing x-ray microanalysis at low energy. Since such operation will, of necessity, rely on the use of L- and M-lines rather than the more familiar K-lines, there is a need for information about the properties of such emissions. Unfortunately even such basic data as the x-ray count rate is hard to

predict because the fluorescent yields for L- and M-lines are poorly documented, and because there are few reliable theoretical or experimental values for the ionization cross-sections of L- and M-line emissions at low energies[2]. We have therefore set out to directly measure and parameterize the absolute X-ray generation efficiencies (photons/electron) for a wide range of K, L, and M lines for different elements which will be the topic for Part-1 of my dissertation under low energy X-ray spectroscopy.

One challenge of X-ray microanalysis at ultra-low beam energies is the reduced count rates which makes it a slow process. For some types of application, such as defect review, a full chemical analysis is more detailed than is needed and that what is actually required is a simple classification of suspect or foreign objects which could be performed at high speed. The use of secondary electron spectra could be a means to this end if a spectrometer incorporating high efficiency and modest resolution could be developed.

Part-2 of the dissertation tests whether or not the secondary electron spectra are influenced by the contaminating surface layers, and determine the nature, and the possible utility, of the secondary electron spectra that might be encountered in a SEM environment.

PART - 1

Low Energy X-Ray Spectroscopy

CHAPTER 1

1.1 Background

In 1948, Raymond Castaing, then a student of A. Guinier, presented to the University of Paris a doctoral thesis entitled: "Application of Electron Beams to a Method of Local Chemical and Crystallographic Analysis." The instrument he described had been produced by modifying an electron microscope. An electron beam focused to a diameter of less than a micrometer ($1\mu m = 10^{-6}m$) was used to excite X-rays within a microscopic region on the specimen surface. Spectral analysis of these X-rays provided information concerning the composition of the excited region.[3] Castaing's electron probe microanalyzer has become the most important tool for elemental microanalysis. The significant characteristics of Castaing's technique are its high spatial resolution, its nondestructive nature, the possibility of quantitative application, the wide range of elements that can be determined, and the variety of specimens that can be analyzed[4]

The physical foundations of electron probe microanalysis were known for years before the work of Castaing. Electron optics of high perfection had been developed for the electron microscope; the basis of X-ray spectrochemical analysis was described in great detail, e.g., in the books of Siegbahn[5] and Von Hevesy[6]. Castaing's brilliant contribution was the skillful combination of known principles in a device which fulfilled an entirely new function. He also established principles for quantitative analysis which are still basically valid and used today. While many persons have since made valuable

contributions to the art of electron probe microanalysis, Castaing is the originator and the most prominent investigator of this technique.

In a wide variety of cases, whether the examples are drawn from fields as diverse as biology or materials science, the macroscopic properties and behavior of the substance are often controlled by chemical structures and processes that take place on the spatial scale of micrometers to nanometers. Electron beam based tools are very useful for such applications as they permit the observation and characterization of materials on such scales. In these instruments the area to be examined or the microvolume to be analyzed is irradiated with a finely focused electron beam which may be static or swept in a raster

across the surface of the specimen. The versatility of scanning electron microscopy and x-ray microanalysis is derived in large measure from the rich variety of interactions that the beam electrons undergo in a specimen. These interactions can reveal information on the specimen's composition, topography, crystallography, electric potential, local magnetic field, and other properties.

Chemical analysis in the scanning electron microscope (SEM) and electron microprobe (EPMA) is performed by measuring the energy and intensity distribution of the x-ray signal generated by a focused electron beam. The major advantage of the x-ray quantitative technique in the SEM and EPMA is that the analysis is obtained from a very small volume of material. The x-rays can be generated, depending on the initial electron-beam energy and atomic number, from volumes with linear dimensions as small as 1 micrometer. This means that, typically, a volume as small as 10^{-12} cm^3 can be analyzed. Assuming a typical density of 7 g/cm^3 for a transition metal, the composition of $7 * 10^{-12}$ g of material can be determined. From this small mass of the sample selected by the

electron - X ray interaction volume, elemental constituents can be determined to concentrations ranging as low as 0.01% (100 ppm), which corresponds to limits of detection in terms of mass of 10^{-16} to 10^{-15} g. Such sensitivities are required because most natural or artificial solid substances are chemically heterogeneous on the microscopic scale [7].

One of the most important contribution of Prof. Raymond Castaing to the technique of X-ray microanalysis was his insight that quantitative microanalysis could only effectively be carried out by procedures which relied on measurements relative to a suitable standard because, in this way, it is the functional variation, rather than the absolute value, of most quantities that had to be known or approximated. At the time, this was seen to be a necessary step because the knowledge of the fundamental parameters of electron-solid interactions was regarded as poor. Regrettably, this situation has not changed much. Even more unfortunately, the kinds of problems to which electron beam microanalysis is now applied – such as the analysis of highly inhomogeneous or very small samples – are of such a nature that quantitative methods based on standardization are no longer feasible.

Consequently, there is a greater need than before to know absolute values of the parameters involved so that ab initio quantification can be attempted.

1.2 X-ray production

During inelastic scattering of the beam electrons, where there is a transfer of energy from the beam electrons to the atoms of the specimen, x-rays can be formed by two distinctly different processes.

1. the bremsstrahlung, or continuous x-ray process, and
2. the inner-shell ionization process, which can lead to the emission of characteristic x-rays.

The production of characteristic x-rays by the bombardment of an atom by an electron can be treated as a two-step process: first, the ionization of the inner shell by the electron; and second, the emission of a characteristic x-ray as the inner-shell vacancy is filled by the transition of an atomic electron from an outer to the inner shell. The first process is characterized by a total cross section for the inner-shell ionization s ; the second process by the fluorescence yield ?, which is defined as the ratio of the rate of x-ray emission to the sum of all possible atomic deexcitation processes. Hence the total x-ray production cross section s_p can be written as $s_p = s_n ?_n$, where n designates the particular inner shell in question [8].

1.3 X-ray Ionization Cross-sections

X-ray ionization cross-sections were first calculated in the 1920s, and an initial attempt at measuring an absolute experimental value was made soon afterwards by Clarke [9]. For the purpose of quantification, it is desirable to know both the absolute magnitude of the cross-section and its functional variation with energy so that the various theoretical models of ionization can be tested and improved. Unfortunately, the number of measurements that have been reported in the past 60 years, for the energy range of interest, is small.

1.3.1 K shells

The best available measurements of ionization cross-sections have been made for the *K*-shells of the low atomic number gases nitrogen, oxygen, and neon. Figure (1.1) shows a compilation of the data for nitrogen (in units of barns where 1 barn = 10^{-24} cm^2/atom), incorporating two distinct published data sets tabulated by Joy[10].The composite plot shows that the various measurements for a given gas typically agree to within a few percent at all energies establishing the cross-sections for these gases, to a high degree of precision and accuracy.

For solids, the amount of data is less, and the agreement between the various available data sets is much worse. As an example, figure (1.2) shows a composite plot from the four published sets of data available for the copper *K*-a line. Most of these sets concentrate on the region immediately above the excitation edge, and here the agreement is seen to be good, but at the higher energies, a clear break between the various results is seen. This is perhaps to be expected because the cross-section can only be extracted after the electron beam interaction with the solid and the subsequent escape of the X-rays, have been calculated in detail. This, in turn, demands knowledge of the electron stopping power and the mass absorption coefficients[11].The apparent differences between different data sets for the same element therefore likely reflect different assumptions about these other parameters and different ways of handling the necessary corrections. In those cases where multiple data sets for the same element have been published, it is quite common to encounter variations of as much as 30 to 50% in absolute cross-section values, even though the general form of the variation with energy is quite similar in each set. Consequently, the absolute value of the cross-section is only known with poor precision.

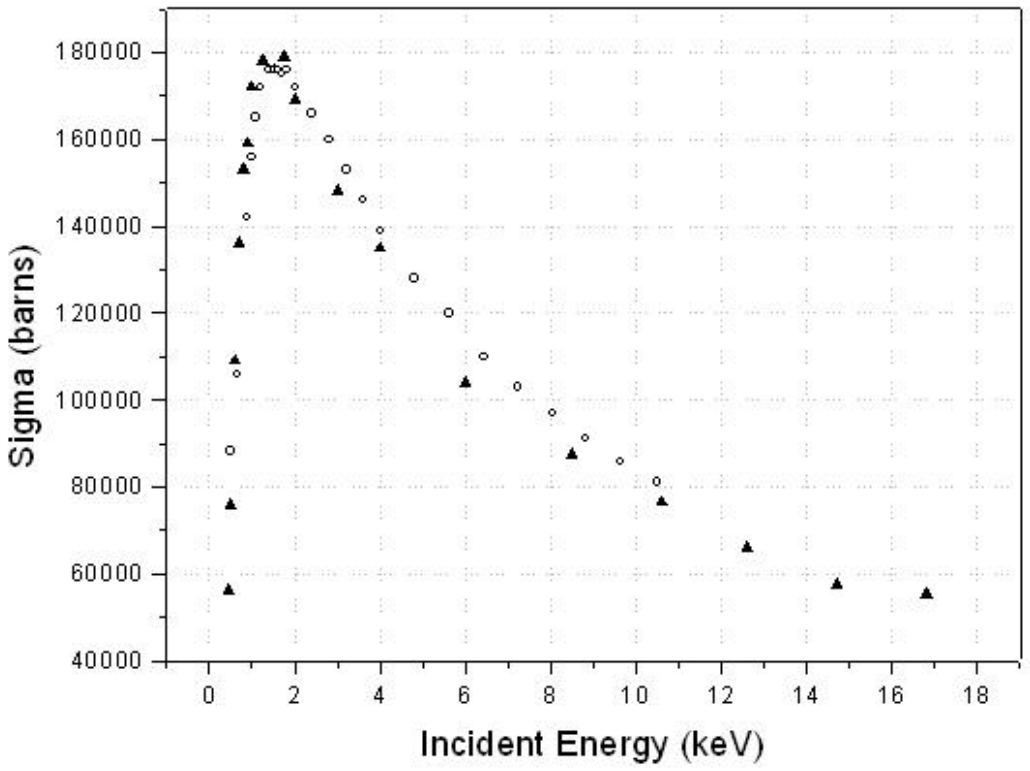

Figure 1.1. A composite plot of the *K* shell X-ray ionization cross-section for gaseous nitrogen as a function of incident electron energy

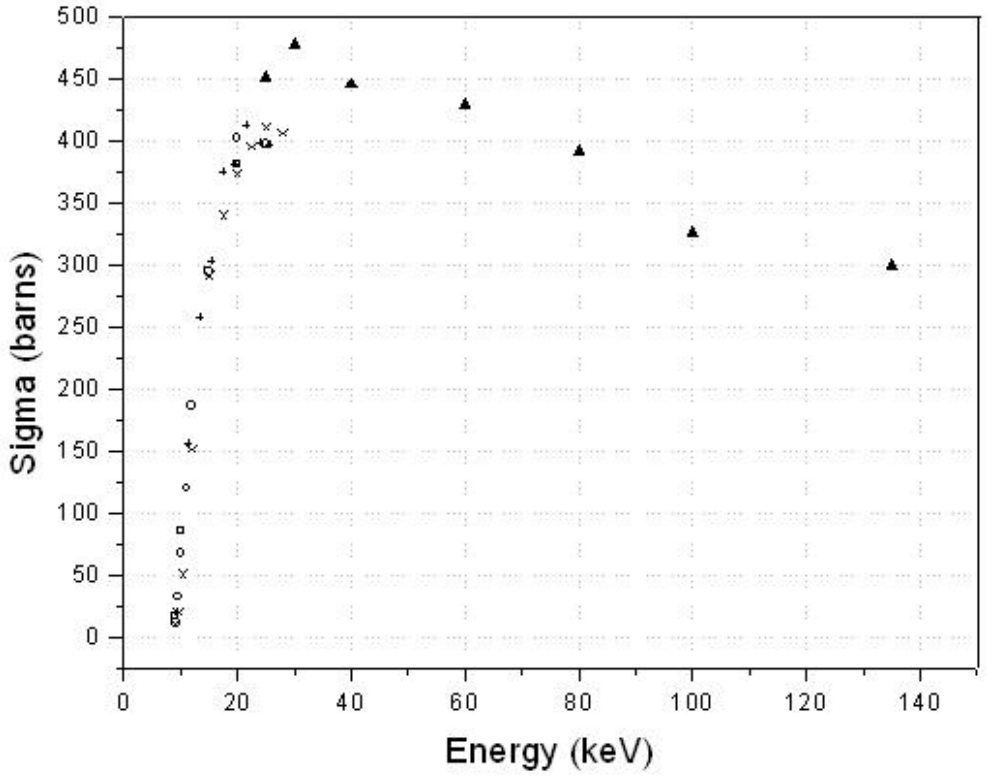

Figure 1.2. A composite plot of measured ionization cross-section data for the copper K-a line showing data from four independent determinations

On the basis of what evidence is available, it appears that the functional variation of *K* cross-sections with energy is different to that suggested by the usual analytical formulae[12]. Since *K* shells ionizations are the preferred choice for microanalysis, it is certainly surprising that only about half of the elements with *K* lines in the energy region of interest have been measured, and in only half of those cases are there more than a single independent set of data points for a given element. Clearly the situation could be described as serious.

1.3.2 L shells

Measured *L* shell ionization cross-sections are available for few elements such as Si, P, S, Cl, Ti, W, Pt and Au – and only in the case of gold are there multiple data sets which can be compared[13]. The reasons for this lack of data are twofold. Historically, *L* lines have been only used as a last resort in quantitative microanalysis and so have been regarded as being of lesser interest. More practically, in order to derive a value for the absolute cross-section, it is necessary to know the fluorescent yield for the line. In the case of *K* lines, as discussed below, this is not a significant problem because good values are available for most of the elements of interest, although the fluorescent yield may not be strictly constant, but vary with the chemical bonding of the element[14]. But for *L* lines, there are some difficult issues to resolve. Firstly, fluorescent yield values are only tabulated for a small number of the elements of interest. Secondly, major corrections have been applied to the measured value to account for Coster-Kronig transitions and so the final result is of poor precision. Such problems in determining the fluorescent yield

have therefore probably inhibited any major effort on measuring ionization cross-sections. Figure (1.3) shows a selection of four of the available *L* line data sets[10], indicating that in addition to these values being unique, and therefore of unknown precision, they only cover a limited energy range which makes it difficult to check the functional variation of the cross-section against theory.

1.3.3 M Shells

There are no published values of *M* shell ionization values for any element with an excitation within the 50 keV energy range. The reasons for this are presumably the same as those discussed as limiting the number of *L* shell values. In particular, the problem of determining a meaningful value for the *M* shell fluorescent yields ? is complex because of multiple non-radiative transitions, and so few serious attempts at measurements are made. Additionally, there is a lack of tested theoretical models against which to benchmark results. With the increased interest in low voltage microanalysis, and the imminent availability of high-resolution spectrometers, however, the need for *M* shell data will increase dramatically and thus some initial experimental work is urgently required.

In summary, measured X-ray ionization cross-sections are only available for a small fraction of the lines of current interest in X-ray microanalysis. Even in most of the cases where data has been published, only a single set of experimental values exists so the accuracy and precision are unknown. Consequently, neither the absolute value nor the functional variation with energy can be satisfactorily established and thus theoretical

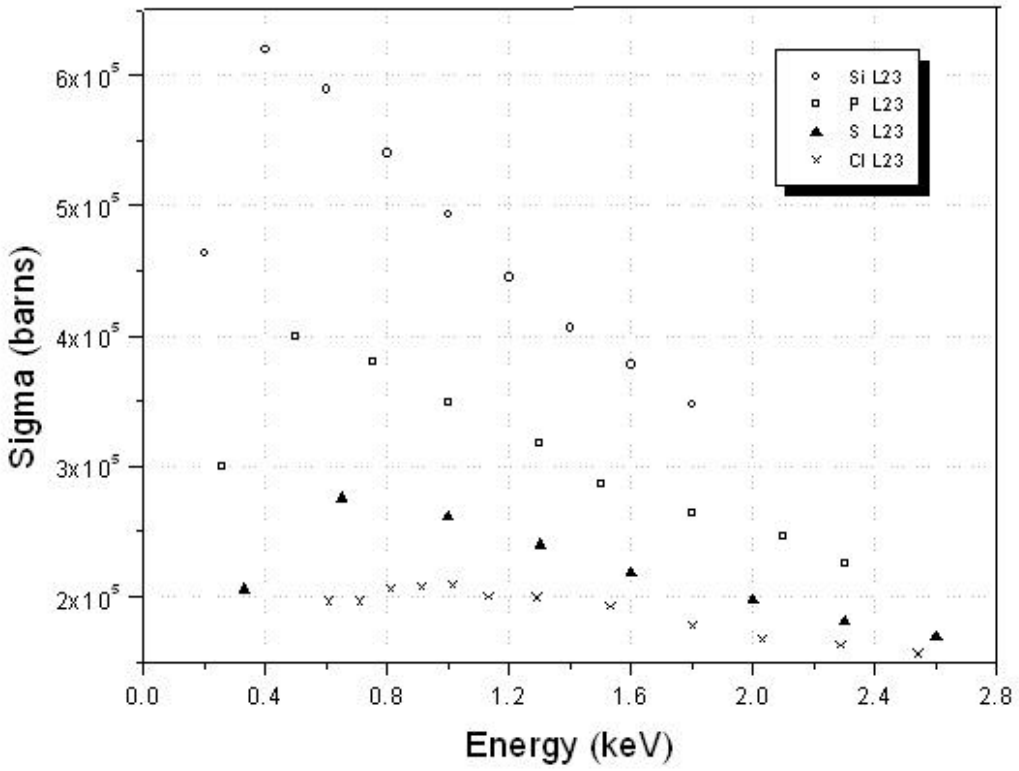

Figure1.3. Measured L shell ionization cross-sections for silicon (Si), phosphorus (P), sulfur (S), and chlorine (Cl)

models cannot be refined. In this situation, it is clear that standardless analysis in any form is, and will remain, a highly incorrect process even for *K* lines.

1.4 Fluorescent Yields

The fluorescent yield ? is the fraction of ionization that results in the production of an X-ray photon. The parameter has not received a great deal of attention because of the assumption that in any analytical method based on standards, the value would not play any part other than in the characteristic fluorescence correction. However, with the increased use of quantification procedures that do not rely on classical standardization methods, and the fact that for *L* and *M* lines the fluorescent yield is not necessarily a constant, there is now a need to know this quantity with some precision.

1.4.1 K Shell Values

The fluorescent yields associated with *K* shell X-ray production have been studied intensively by many workers. Additionally, many authors have exhaustively analyzed this data for rogue values and systematic errors[15, 16]. Figure (1.4) shows a composite plot of their data values covering the atomic number range from 11 to 94 and including all but about half a dozen of the possible elements. The curve is seen to be smooth and monotonic, and the data points have a relative precision estimated to be better than 5%. Given that the measurement of fluorescent yields is a difficult procedure often involving a comparison of two techniques, such as Auger and X-ray excitations, each of which has significant counting error associated with it, this is a remarkable achievement. In fact, as

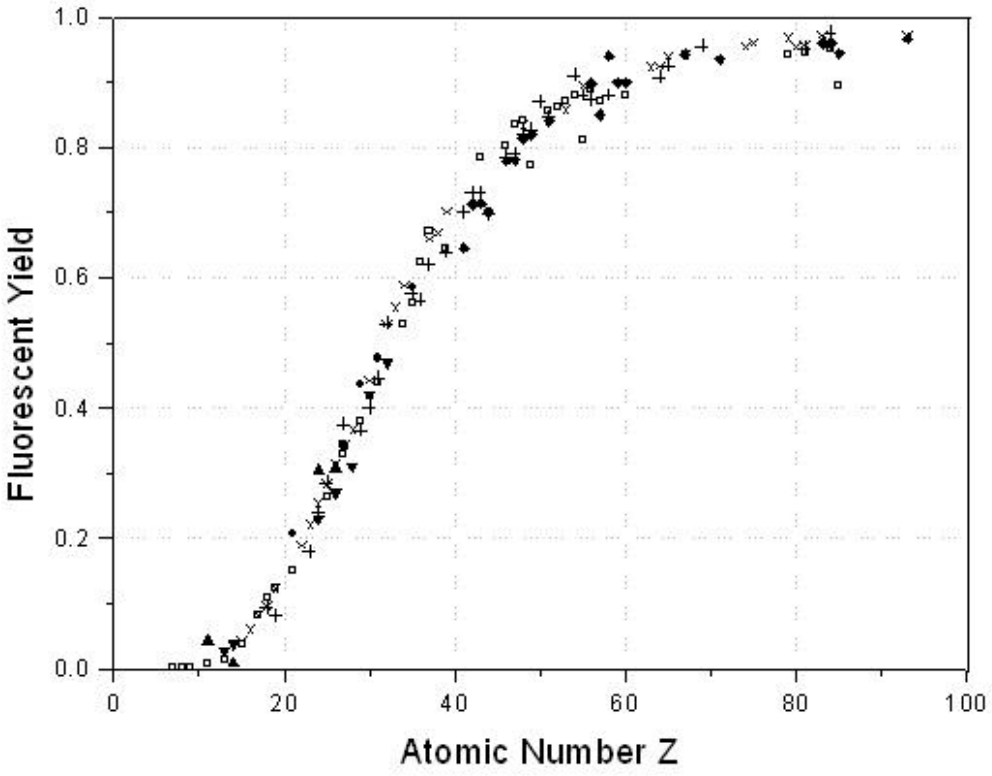

Figure 1.4. A composite plot of published data for the fluorescent yield of K shell ionizations as a function of atomic number

a result of this effort, the *K*-shell fluorescent yields are probably the best documented of all the constants required for microanalysis.

1.4.2 L Shell Values

The situation for *L*-shells is less satisfactory as shown in figure (1.5). Significantly less data has been published, and these values have not been as carefully refined. Yields for elements from atomic number 40 through to 94 have been published but there are several gaps and the relative scatter in the data is much higher than for the *K* shells. This can be attributed to the different corrections that authors have made for Coster-Kronig transitions in each case[16]. Since this correction is typically about equal in magnitude to the fluorescent yield itself, the error introduced by this step is obviously high. Changes in the chemical bonding of the element of interest may also alter the corrections that have to be applied, so leading to further imprecision in the result.

1.4.3 M Shell Values

The problems that are evident with the *L* shells are even more pronounced for the *M* shells as shown in figure (1.6). Data has only been published for five elements[10], all of high atomic number, and the magnitude of the corrections that have to be applied for non-radiative transitions is much higher than the final derived value of ?, so the precision of the result can be expected to be poor. The evidence also shows that the effective variation of ? with chemistry is large and unpredictable so that the published values can only safely be taken to apply to the element in the form in which it was measured.

In summary, fluorescent yield data is of variable quality and quantity. In addition to the obvious impact on first principle calculations of the shortcomings of the data, problems in

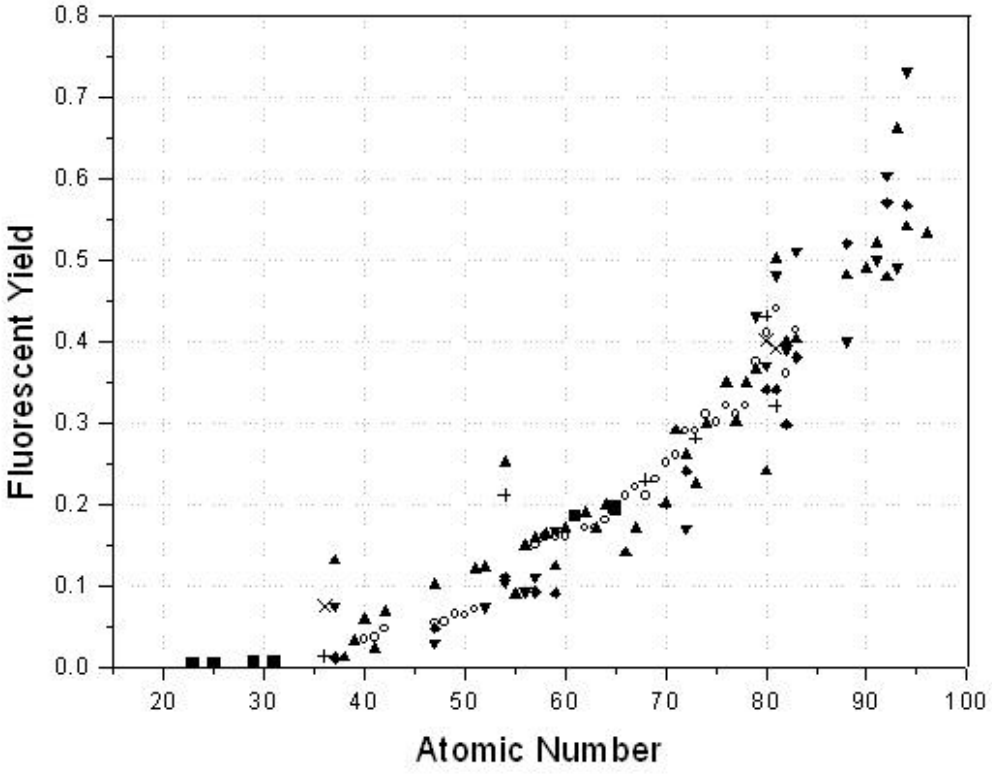

Figure 1.5. A composite plot of published data for the fluorescent yield of *L* shell ionizations as a function of atomic number

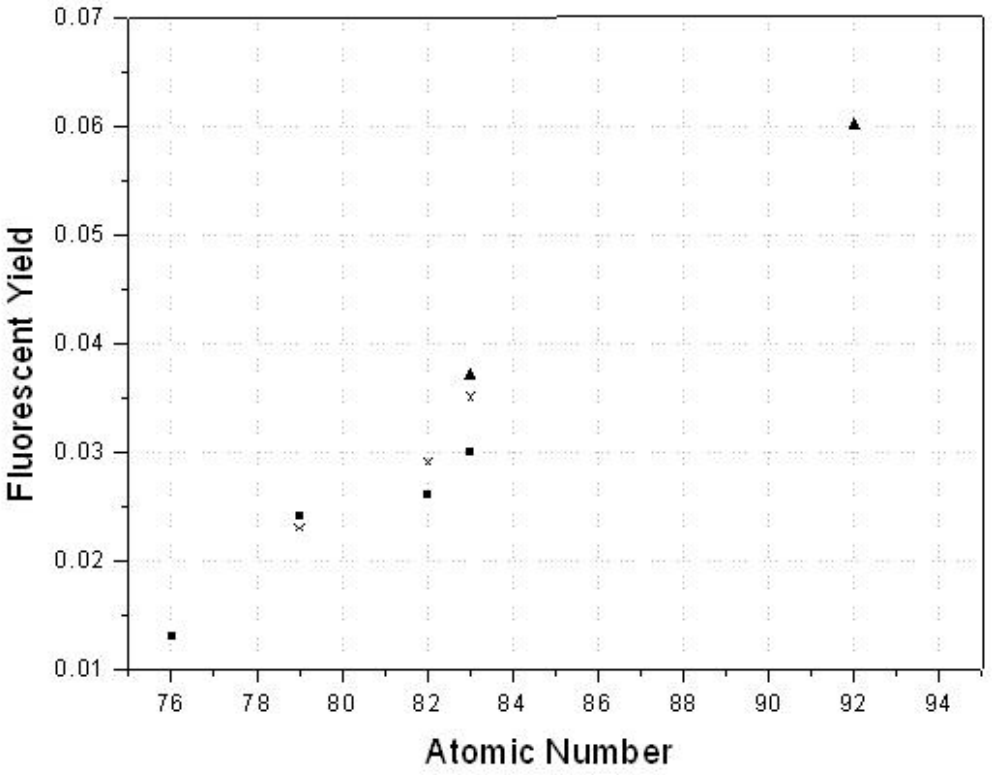

Figure 1.6. Measured fluorescent yield data for *M* lines as a function of atomic number

our ability to accurately define values for the *L* and *M* shells fluorescent yields, ?, means that attempts to determine ionization cross-section values, s, will also be compromised if X-ray-based measurement methods are employed since the production of photons varies as s?. When the s and ? values are later recombined in a calculation, the already large errors in each of the quantities are further increased.

1.5 Better Approach

A more useful approach is to abandon the effort to separate these variables and to work instead with the absolute X-ray generation efficiency (photons per steradian per electron) since this is what determines detectable X-ray production. Several sets of measurements of X-ray generation efficiency have been reported and these results show that for *K*, *L*, and *M* lines, the yield $?_{x\text{-}ray}$ can be expressed in the form [17,18]

$$?_{x\text{-}ray}(U) = ?_0 (U-1)^n$$

where $?_0$ is a constant for each element and line, U is the over-voltage ratio, and the exponent n has a value between 1.55 and 1.67.

A major part of the work described in this thesis seeks to extend and improve our knowledge of the magnitude and functional variation of the absolute X-ray yield.

CHAPTER 2

2.1 The Generation of Characteristic Primary X-rays

The intensity of X-ray emission from a target bombarded by electrons depends on the interrelationship of the processes of electron deceleration and scattering and ionization. The ionization of an inner shell which is required for the emission of an X-ray photon is a relatively rare event. Most of the electron energy is spent in interactions with outer, weakly bound orbital electrons. The primary electron thus suffers a large number of small energy losses which are usually described as a quasi-continuous deceleration. Only a small fraction of the primary electrons produce an X-ray photon.

The probability of ionization of an inner shell depends on the energy of the penetrating electron, which diminishes along its path within the specimen. After the energy of the primary electron has dropped below the critical excitation potential of a given inner shell, no further ionization of this shell can occur. Therefore, the X-ray lines produced by this shell can no longer be excited. Interactions of the beam electrons with an atom also include large changes in direction of the electron (large-angle scattering). Some of the scattered electrons reemerge from the specimen surface, before their energy has dropped below the critical excitation potential. The backscattering of electrons reduces the number of inner-shell ionizations with respect to that which would be observed if all primary electrons had remained within the target (see Figure 2.1)[4].

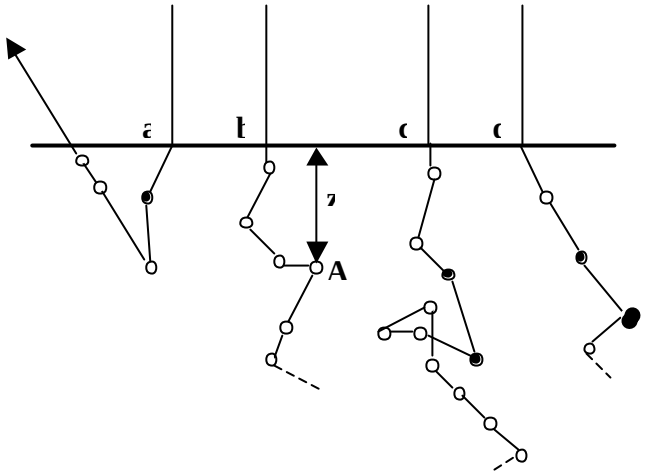

Figure 2.1. Schematic representation of collisions within the target.

The first electron at the left (at 'a') shows large-angle scattering at the second collision and subsequent backscattering. The dark circle at the path at the right represents an ionization in an inner orbit which may cause the emission of a characteristic X-ray photon. Note (second path from left [at 'b']) that the path from the surface to point A is larger than the depth of penetration, z. Dotted paths correspond to electrons which do not have sufficient kinetic energy left to produce ionization of the inner orbit of interest.

In order to calculate the average number of primary characteristic photons of a line produced by one electron along its trajectory within the specimen, we must therefore quantitatively describe:

a) the loss of energy of the electron along its path in the target (stopping power);
b) the probability of ionization of the inner shells of target atoms, as a function of the energy of the ionizing atom (ionization cross section);
c) the loss of X-ray production caused by electron backscatter (electron backscatter correction factor);
d) the probability of photon emission of the line of interest subsequent to ionization of the corresponding shell (fluorescent yield, weight of X-ray line).

2.1.1 Electron Stopping Power

If we regard the deceleration of the beam electron within the target as a continuous process, we can express the average rate of energy loss by means of the equation:

$$-dE = S\, ds \tag{2.1}$$

The symbol E denotes the energy of the electron at any point of the path. For a small energy loss, the energy diminishes proportionally to the number of atoms in the way of the electron, and thus to the mass thickness, ds (g/cm^2). The proportionality factor, S, is called stopping power ($eVg^{-1}cm^2$ or eV per angstrom). Equation (2.1) relates energy loss to the actual length of path, s, rather than to depth beneath the surface, z. This distinction

is necessary, since, due to scattering, the path of the electron is larger than the depth *z* (Figure 2.1).

The magnitude and variation of the stopping power (SP) determines the range of the incident electron, as well as the lateral and depth distribution of the X-ray ionization. Hence it is an important factor in determining the spatial resolution of the analysis, as well as the magnitude of the absorption, fluorescence, and backscattering corrections. Despite the importance of SP in any quantification procedure, microanalysts have generally been content to derive estimates of magnitude from the equation given by Bethe (1930)[19] :

$$\frac{dE}{dS} = -78{,}500 * r \frac{Z}{AE} * \ln\left(\frac{1.166E}{J}\right) \qquad (2.2)$$

where E is the energy of the electron (in keV), Z and A are, respectively, the atomic number and atomic weight of the target, ? is the density of the target, and s is the distance measured along the electron trajectory. *J*, which has units of keV, is the mean ionization potential and represents the effective average energy loss per ionization. Values of *J* have been obtained from high energy beta particle experiments (ICRU, 1983)[20] and for a pure element of atomic number Z are often represented by the approximation of Berger and Seltzer[21]

$$J = \left[9.76Z + \frac{58.5}{Z^{0.19}}\right] * 10^{-3}(keV) \qquad (2.3)$$

The main attraction of the Bethe model is that the behavior of the material is represented by a single parameter, *J*. However, the Bethe equation is only likely to be valid for energies E greater than at least the *K* shell excitation energy of the material. For all lower energies, *J* is variable, and the equation itself becomes non-physical for E< 0.85*J*. Many attempts have been made to overcome these limitations, for example rewriting equation (2.2) in the form (Joy and Luo, 1989)[22] :

$$\frac{dE}{dS} = -78{,}500 * r\frac{Z}{AE} * \ln\left(\frac{1.166(E + 0.85J)}{J}\right) \qquad (2.4)$$

extends the range of application of the equation and provides improved low energy behavior[11]. Experimental SP profiles have been obtained by direct measurements of energy losses in thin foils (Garber et al., 1971)[23], by calorimetry (Al-Ahmad and Watt, 1983)[24], and by extracting the energy loss function from electron energy loss spectra (EELS)[25]. More experimental stopping power curves can be found in our database[10] and Joy *et.al.*, 1996[26].

2.1.2 Ionization Cross section

If a thin layer of an elemental target material is crossed perpendicularly by *i* electrons, the number of ionizations, *n*, of electrons in the shell *q*, of the target atoms is proportional to the number of atoms present, *N*, to that of the electrons which cross the layer, and inversely proportional to the area *a* over which the *N* atoms are uniformly distributed:

$$n = Q_q N i a^{-1} \tag{2.5}$$

The atomic ionization cross section, Q_q , for the shell q has the dimensions of an area. If we consider a layer of material of thickness dx (g / cm^2), the number of atoms in this layer is equal to

$$\frac{N_{av}}{A} * a * dx \tag{2.6}$$

so that the number of ionizations occurring when i electrons cross the layer is equal to

$$dn = Q_q i \frac{N_{av}}{A} dx \tag{2.7}$$

Most experimental and theoretical investigations of ionization cross sections concern *K*-shell. This subject has been discussed in detail in Green's thesis[27], and by Powell[12]. As discussed by Powell, Bethe provided a theoretical formula which can be brought into agreement with experimental data:

$$Q_q E_q^2 = 6.51 \times 10^{-14} * z_q * b_q * \frac{\ln\left(c_q * U\right)}{U} cm^2.eV^2 \tag{2.8}$$

The term z_q denotes the number of orbital electrons present in the filled shell – or subshell – q, the ionization of which leads to the emission of the line of interest. The values of z_q for the shells of main interest are given in Table 2.1.

Table 2.1 Number of Electrons in the Filled Shell[4]

Level	Important Lines	z_q
K	$K_{a1,2}$, $K_{ß1}$	2
$L_?$	$L_{ß3}$	2
$L_{??}$	$L_{ß1}$	2
$L_{???}$	$L_{a1,2}$	4
M_V	M_a	6

The overvoltage, $U = E / E_q$, is the ratio of the instantaneous energy of the electron at each point of the trajectory to that required to ionize the level *q*. The values of B_q, b_q, and c_q are constants which presumably are independent of the target. Powell fitted equation (2.8) to the experimental and calculated cross sections for overvoltages above five from several investigators. He obtained fits for pairs of values of b_q and c_q, for the *K*- and *L*-shells, which are, in general, within the following limits:

	b_q	c_q
K-shell	0.7-1.0	0.6-1.0
L-shell	0.5-1.0	0.5-0.9

A simplified equation is given by Green and Cosslett[28], and derived from the work of Worthington and Tomlin[29]:

$$Q_q = 7.92 \times 10^{-20} E_q^{-2} \frac{\ln U}{U} \tag{2.9}$$

Powell[30] in a review of expressions for the ionization cross section recommends, for overvoltages from 1.5 to 25, a modification by Fabre[31] of the Bethe equation:

$$Q_q * E_q^2 = \frac{6.51 \times 10^{-14} z_q * \ln(U_q)}{a_q(U_q + b_q)} cm^2 eV^2 \tag{2.10}$$

in which a_k = 1.18 and b_k = 1.32. Moreover, empirical and semi-empirical cross section formulae have also been proposed and are widely used in applied work[32, 33]

2.1.3 Simple Approximations for Primary X-ray Intensities

Whiddington[34] proposed the following model for the energy of a penetrating electron:

$$S = -dE/ds = \text{constant}/E \tag{2.11}$$

Hence,

$$E_0^2 - E^2 = c * s \tag{2.12}$$

with s given in grams per square centimeter. It was later found that the constant c changes slowly with the energy of the penetrating electron as shown in table 2.2.

Table 2.2. Values of *c* as a function of electron energy[4]

E (keV)	c ($keV^2 cm^2 g^{-1}$)
1	$1*10^5$
2	$1.3*10^5$
5	$1.8*10^5$
10	$2.3*10^5$
20	$2.9*10^5$
50	$4.4*10^5$

Combining equation (2.12) with Bethe's law for ionization cross sections (equation 2.7) and considering that the number of ionizations per electron is equal to

$$n_q = -R\int_{E_q}^{E_0} \frac{N_{av}}{A} \cdot Q \cdot \frac{ds}{dE}\, dE \tag{2.13}$$

we obtain the following expression[28]

$$n_k(direct) = 9.54\times10^4 \frac{R}{Ac}\left[U_0 \ln U_0 - (U_0 - 1)\right] \tag{2.14}$$

for the generation of K-lines. In addition to the direct contribution, Green and Cosslett[28] calculated the following contribution due to indirect excitation, which is caused by the X-ray continuum:

$$n_k(indirect) = 1.46\times10^{-8}(z-2)^2 z\left[U_0 \ln U_0 - (U_0 - 1)\right] \tag{2.15}$$

The direct and indirect contributions to core shell ionization were then combined and multiplied by the fluorescent yield W_k, to give the following expression for the total X-ray yield:

$$\frac{N_k}{4p} = W_k\left(9.54\times10^4 \frac{R}{Ac} + 1.46\times10^{-8}(z-2)^2 z\right)\times\left[U_0 \ln U_0 - (U_0 - 1)\right] \tag{2.16}$$

Furthermore, incorporation of the approximation

$$U_0 \ln U_0 - (U_0 - 1) \approx 0.365(U_0 - 1)^{1.67} \qquad (2.17)$$

proposed by Duncumb[35] gives:

$$\frac{N_k}{4p} = W_k\left(2.80\times10^{3}\frac{R}{Ac} + 4.27\times10^{-10}(z-2)^2 z\right)\times\left[(U_0 - 1)^{1.67}\right] \qquad (2.18)$$

It is at this point that one sees the theoretical justification for the 1.67 power dependence commonly used to support some experimental observations. However, equation (2.18) is applied only to the X-ray signal as generated within a specimen. Further corrections for Specimen observation are required, to relate this expression to what is actually observed[18].

2.2 The Absorption of Primary X-rays

The primary absorption factor f_p is the fraction of the radiation directed toward the X-ray detector which remains after emergence from the surface. It is strongly affected by the penetration of the electron beam, which in turn depends on the operating potential, V_0, the angle of observation of the X-rays (X-ray emergence angle ?), and the composition of the target which determines its X-ray absorption coefficient. The absorption loss can be

small (f_p ~ 1), or, depending on the above mentioned parameters, it can be severe, and thus introduce serious uncertainty in the analytical result. Errors in the estimate of f_p are, in fact, the most significant cause for inaccuracy of the analysis. For this reason, the accurate determination of the primary X-ray absorption factor is of great importance. Figure 2.2 shows schematically the emergence of the primary X-rays which, are emitted from a roughly spherical region. The intensity distribution of the generation of primary X-rays as a function of depth *z*, is shown at the left side of the figure. The function which expresses this depth distribution is called ? (z). Depth is usually measured in linear units such as micrometers. z (mg/cm^2) denotes mass thickness.

The characteristic X-rays generated within the specimen propagate isotropically in all directions. Hence, if the energy-dispersive spectrometer subtended an angle O, then a fraction of primary X-rays generated at any given point, equal to (O/4?).I_p (where I_p is the average number of characteristic primary X-ray photons of the line of interest produced within the specimen by one impinging electron), moves toward the detector. The mean angle of emergence of the X-rays is ?, but in reality the emergence angles cover a range which is determined by the aperture of the detector.

2.2.1 Determining the absorption factor, f (?)

Since the X-rays produced by the primary beam are created at some nonzero depth in the specimen (see figure 2.3), they must pass through the specimen on their way to the detector. On this journey, some of the X-rays undergo photoelectric absorption because of interactions with the atoms of the various elements in the sample. Following the initial formulation of Castaing (1951)[3], the intensity dI_i of characteristic radiation, without

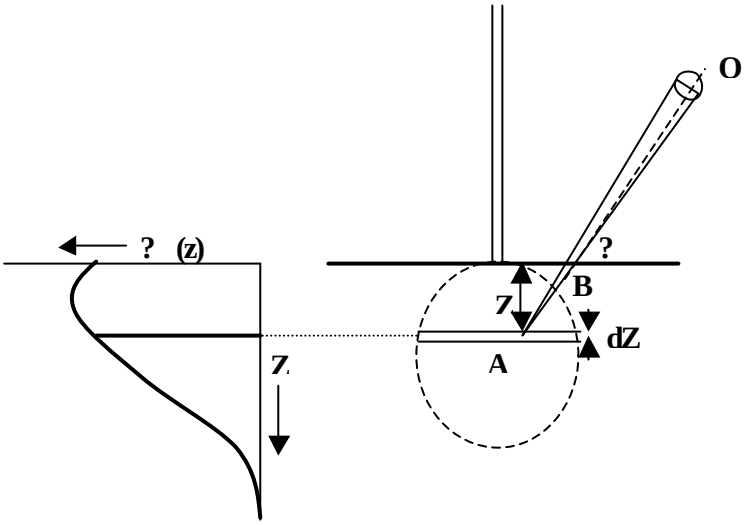

Figure 2.2 Distribution in depth of generation of primary X-ray photons. The X-rays emerging at an angle ? from the specimen surface, and contained within a small solid angle, O, reach the detector. On their path within the target (from A to B), some photons are absorbed.

a)

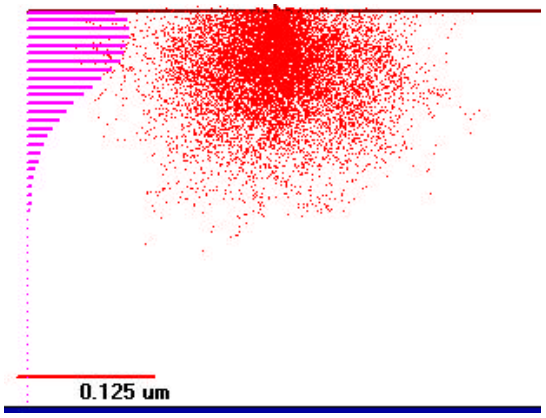

b)

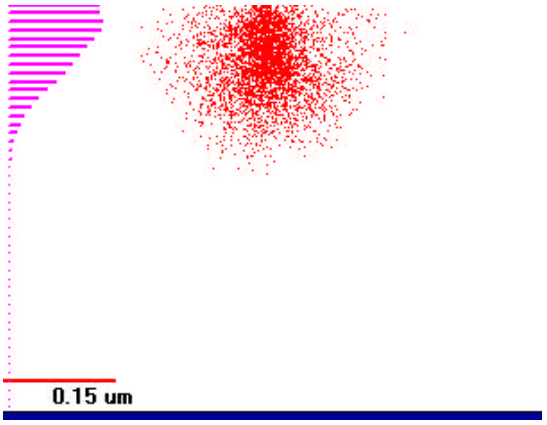

c)

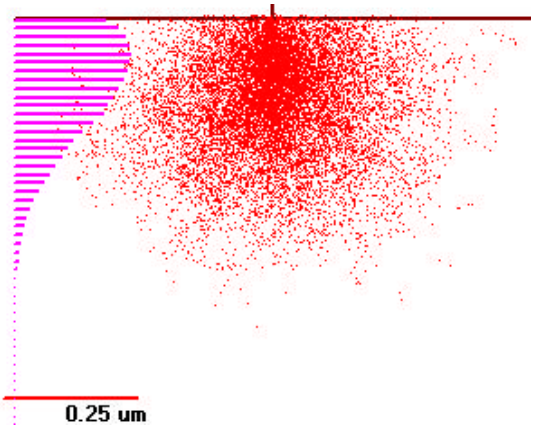

Figure 2.3 X-ray production depth for a) Au M-line b) Fe K-line c) Zr L-line at 10keV

absorption, generated from element *i* in a layer of thickness *dz* having density ? at some depth *z* below the specimen surface is

$$dI_i = I_i(\Delta rz) f_i(rz) d(rz) \tag{2.19}$$

where $?_i(?z)$ is defined as the distribution of characteristic X-ray production of element i with depth and I_i (? ?z) is the X-ray intensity of an isolated thin film. In the absence of absorption, the total flux generated for element *i*, I_{igen}, is

$$I_{igen} = I_i(\Delta rz) \int_0^\infty f_i(rz) d(rz) \tag{2.20}$$

Considering absorption of the generated X-rays, the total flux I_{iem} emitted is

$$I_{iem} = I_i(\Delta rz) \int_0^\infty f_i(rz) \exp -[(m/r)^i \csc y\,(rz)] d(rz) \tag{2.21}$$

where $(\mu/?)^i$ is the X-ray mass attenuation coefficient of the specimen for the characteristic X-ray line of element *i* and ? is the take-off angle, the angle between the direction of the measured X-ray and the sample surface (figure 2.2).

The quantity $(\mu/?)^i$ csc ? is called ?. Philibert (1963)[36] referred to the generated intensity I_{igen} as $F(0)$, when ? is zero. He also referred to the emitted intensity I_{iem} as $F(?)$. Using these terms, the ratio $F(?)/F(0)$ is called $f(?)$, which is equivalent to

$$f(c) = \frac{\int_0^{\infty} f_i(rz)\exp-[(m/r)^i \csc y\,(rz)]d(rz)}{\int_0^{\infty} f_i(rz)d(rz)} \qquad (2.22)$$

The ratio *f*(?) is called the *standard absorption term*[36].

For the determination of the absorption correction A_i for any element *i* in a composite specimen, we use the equation

$$A_i = \frac{f(c)_{std}}{f(c)_{spec}} \qquad (2.23)$$

The absorption correction factor *f*(?) of a specific characteristic line of element *i* depends on the respective mass absorption coefficient μ/?, the X-ray emergence angle ?, the initial energy of the electron beam E_o, the critical excitation energy E_c for K, L, or M radiation from element *I*, and the mean atomic number and mean atomic weight of the specimen. Hence we can write

$$f(c) = f[(m/r)\csc y, E_o, E_c, \overline{Z}, \overline{A}] \qquad (2.23)$$

The most commonly used absorption correction, that of Philibert-Duncumb-Heinrich, was developed by using an empirical expression for ?(?z)[37].

CHAPTER 3

3.1 Current state

Electron bombardment of a solid target is the most important practical method of generating characteristic X-rays, but, until recently, few measurements of the efficiency of this process had been made, especially at low beam energies. The rate of generation of X-rays from an element irradiated at some energy E depends on the product of the ionization cross-section $\sigma(E)$ and the fluorescent yield ω. Unfortunately neither of these quantities is well established independently, especially outside of the K-series of lines (For a complete listing of experimental σ and ω values see http://pciserver.bio.utk.edu/metrology). Even such basic data as the X-ray count rate is hard to predict because the fluorescent yields for *L* and *M* lines are poorly documented, and because there are few reliable theoretical or experimental values for the ionization cross-sections of *L* and *M* line emissions. This poses a challenge especially when performing X-ray microanalysis at low energies since such operation will rely on the use of *L* and *M* lines rather than the more familiar *K* lines[2]. A search of the literature has revealed no early *L* and *M* series measurements although absolute *L*-shell ionization cross sections have been reported for a few elements such as Ar[38, 39], Kr[8], Xe[8, 40], Au[41, 42, 43, 44], and W[45] (See also Refs. 2 , 46, 47). Inspection of the currently available experimental data reveals that they are still scarce for many elements and, when they are available, one usually finds significant discrepancies between data from different authors, which are

often much larger than the stated experimental uncertainties[12, 48]. The situation is even worse for *M* shells, for which experimental data are extremely rare. New, accurate experimental measurements of *L*- and *M*- shell ionization cross-sections by electron impact are therefore urgently needed.

3.2 Challenges in determining inner-shell ionization cross-sections

The determination of absolute values of the cross-section for *L* and *M* shells, however, poses numerous difficulties due to the fact that vacancies in a given subshell can be produced not only by electron impact but also by nonradiative (Coster-Kronig) transitions between the subshells. As a consequence, the intensity of a given x-ray line depends on the ionization cross sections of all the subshells, weighted by the corresponding Coster-Kronig coefficients. Consequently, to determine subshell ionization cross sections we have to measure the intensities of a number of x-ray lines, some of which may not be clearly resolved or may have very low intensities. Moreover, Coster-kronig coefficients are generally affected by large uncertainties, which would propagate to the derived ionization cross sections.

3.3 Advantages of measuring absolute X-ray generation efficiencies

Considering these difficulties, it is advisable to report the generation efficiency of X-rays, usually for the most intense lines, rather than the cross-section for inner-shell ionization.

By proceeding in this way, Coster-Kronig coefficients, fluorescence yields, and fractional emission rates do not affect the reported experimental data. It should also be noted that for many applications, including electron probe microanalysis, the goal is to calculate X-ray intensities from irradiated samples, which can be obtained from knowledge of the cross section for X-ray production[13]. We have therefore set out to directly measure and parameterize the absolute X-ray generation efficiencies (photons /electron) for a wide range of K, L, and M lines from different elements. All of these lines, with the exception of the Cu K, have a critical excitation energy E_{crit} lower than 2.6 keV and are thus suitable for low-energy microanalysis. A complete set of such data would be of great value in applications such as spectrum simulation and standardless analysis.

During the first half of the present century a small number of workers, including Wisshak (1930)[49], Braxton *et al.* (1945)[50] and Kirkpatrick and Baez (1947)[51], Dyson (1959)[52], Dolby (1960)[53], Campbell (1963)[54], Metchnik and Tomlin (1963)[55], Hink (1964)[56] and Brown and Oglivie (1964)[57] have published experimental efficiency values for the K series. Hink (1965)[58] and Green and Cosslett (1968)[17] have reported efficiency measurement for the L series. The accuracy of the measurements described was limited by the choice of the detection schemes then available; namely, proportional counters or Ross filters used in combination with scintillation counters. Specifically, data reduction problems arose from uncertainties encountered in the determination of the shape and

magnitude of the x-ray continuum background. It is this quantity that must be subtracted from the measured peak value in order to give characteristic line intensities. If an ideal detection system (one with energy resolution better than the line width and 100% efficiency for all measured energies) were available, then peak-to-background

measurements would be straightforward, Even at low overvoltages, the peak-to-background ratio would be high and backgrounds could be determined by interpolating between points a few electron volts above and below the peak value. Energy dispersive spectroscopy has excellent potential for such measurements because the method is characterized by a high collection efficiency (approaching 100% in the 2 to 20 keV range) and good energy resolution, and the solid angle subtended by the detector can be accurately determined.

3.4 Energy-Dispersive Spectroscopy

An EDS system is comprised of three basic components that must be designed to work together to achieve optimum results.

X-ray Detector: Detects and converts X-rays into electronic signals

Pulse Processor: Measures the electronic signals to determine the energy of each X-ray detected

Analyzer: Displays and interprets the X-ray data.

The EDS detector converts the energy of each individual X-ray into a voltage signal of proportional size. This is achieved through a three stage process. Firstly the X-ray is converted into a charge by the ionization of atoms in the semiconductor crystal. When an incident X-ray strikes the detector diode (usually a Si P-I-N device), its energy is absorbed by a series of ionizations within the semiconductor to create a number of electron-hole pairs. The electrons are raised into conduction band of the semiconductor

and are free to move within the crystal lattice. When an electron is raised into the conduction band it leaves behind a 'hole', which behaves like a free positive charge within the crystal. A high bias voltage, applied between electrical contacts on the front face and back of the crystal, then sweeps the electrons and holes to these opposite electrodes, producing a charge signal, the size of which is directly proportional to the energy of the incident X-ray. The conversion of an X-ray to a charge occurs very quickly so many X-rays can be measured each second[59].

Secondly this charge is converted into the voltage signal by the Field Effect Transistor (FET) preamplifier (see figure 3.1). The output of the FET is a 'staircase' in which the height of each step is proportional to the energy of the last X-ray detected. The staircase is differentiated and shaped to give a Gaussian pulse whose area represents the X-ray energy. The more time spent shaping the pulse, the more accurate the energy measurement. At the same time electronic noise must be minimized to allow detection of the lowest X-ray energies. The staircase is reset from time to time to prevent overload. Finally the pulses from the preamplifier are digitized by the ADC (Analog-Digital Converter) where the number output is used as an address (0-1024). One count is then added to the channel with that address and the histogram of counts versus channel number is plotted periodically to produce the spectrum.

3.4.1 Resolution

The performance of the EDS detector is measured by its resolution – the full width of the peak at half its maximum height (FWHM). The resolution is a property of the detector

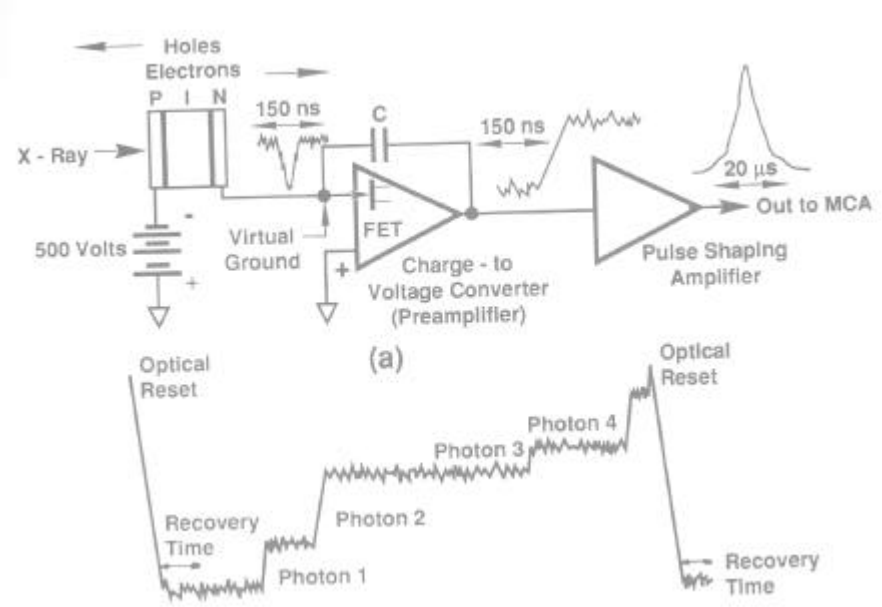

Figure 3.1. Charge-to-voltage conversion process.

(Courtesy: Goldstein *et al., Scanning Electron Microscopy and X-ray Microanalysis,* 2nd edition, p297.)

but the actual value depends on the energy of the X-ray measured. The specified value at Mn K-a photons (5.9keV) for the detector used is 139 eV. The resolution depends on detector size but is also limited by how well the pulses have been shaped by the processor. Accurate shaping takes a long time so we must compromise between count rate and resolution. Longer times give better peak to background ratios.

3.4.2 Deadtime

The process time t sets the resolution. If it is set to be long then because Multi-Channel Analyzers only handle one pulse at a time some pulses will be missed. This 'dead time' is allowed for by increasing the time allowed for the analysis. Based on the dead time, the machine computes how much real time must be taken to collect for a given live time.

If N pulses are processed /sec and each takes t then

Dead time = Nt

Fractional loss = 1 – Nt

Live time = Clock time / (1- Nt)

For the experiment the dead time was maintained at 25% so we lose (1-0.25) = 0.75 of the incoming X-rays and a 100sec (Live time) analysis took 133 sec (clock time) on the clock. Deadtime increases with count rate (beam current and energy) and process time.

3.5 Experimental Procedure

The measurements and the subsequent analysis of the data are a development of the approach first described in classic papers by Campbell[54] , Green & Cosslett[17] and Lifshin

et al[18]. The experiment consists of a measurement of the emission rate in counts per picoampere of beam current per second. The majority of the elements examined were part of a microprobe standards block. The block contains fragments of each of a number of elements embedded in epoxy and finished with highly polished flat surfaces and Faraday cup for the beam current measurements. The microscope was a Hitachi S-3500 thermionic emission gun SEM (Hitachi High Technologies America, Pleasanton: CA) equipped with a Gresham EDS detector (4 Pi Inc: Raleigh, NC) with an energy resolution of 139 eV. The multichannel analyzer was an Apple Macintosh based system controlled by the N.I.S.T software package DTSA – Desktop Spectrum Analyzer[60] (Fiori et al., 1992).

The SEM was equipped with a Deben 'Sprite' automated stage which made it possible to move rapidly between different element areas on the block and the Faraday cup location to check the beam current, and also made it possible to maintain precisely the geometry of the experiment to ensure that the detector take-off angle (35[?]) and the solid angle subtended by the detector at the sample were held constant (figure 3.2).Measurements were made for live-time period of 100 s and several such measurements were averaged at each energy. The beam current was measured immediately before and after each run using a Keithley 414A picoammeter and was adjusted over the range 80pA to 1.2nA to maintain an approximately constant count rate with energy. This current was enough to generate 20,000 – 100,000 counts for each peak to ensure good statistics except for very

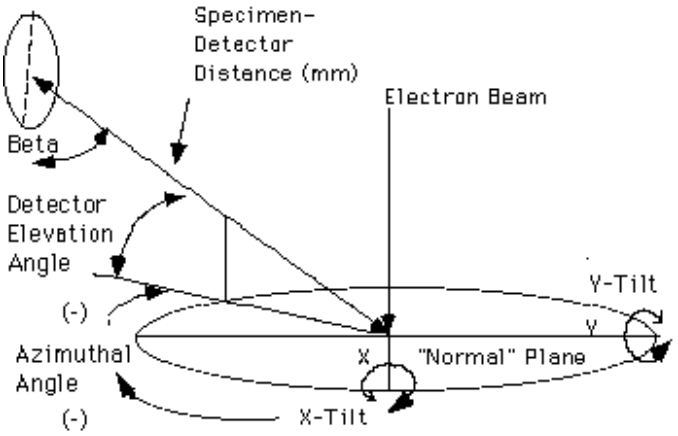

Figure 3.2. Detector – Specimen geometry.

The electron beam is perpendicular to the 'Normal' Plane. All angles except Beta are with respect to this plane. Beta is the angle between the detector surface and the arrow from the specimen. In the usual geometry it is 90 degrees. Azimuth as shown is about -135?.

low overvoltages. The net intensity of the chosen X-ray line was obtained by using a DTSA background subtraction routine which uses a "Free Quadratic" model, a second degree energy polynomial that has extra freedom to cause a "good" fit over a wide energy range

3.5.1 Background correction

Two or more "Background ROI's (regions of interest)" are required to be judiciously set-up in peak and artifact free regions of the spectrum for which it is desired to remove the background. The ROI's were chosen to be near the peak (e.g., one ROI on each side of the peak). Since incomplete charge collection can cause a distortion on the low energy side of a peak, especially in the 3-5 keV range, the low energy ROI was placed asymmetrically further from the peak than the high energy ROI (that can be placed quite close to the peak). Then a linear background subtraction method was used to get the net intensity of the peak. Figure 33 illustrates this method for a tungsten (W) Ma line at an incident beam energy of 5keV (U = 5 / 1.775 = 2.82). As shown in figure,

The peak intensity (169 – 194 eV channel) = 131142 counts

Left ROI (160 – 165 eV channel) = 4077 counts

Right ROI (195 – 200 eV channel) = 2864 counts

Net intensity = 131142 – 25(4077 + 2864)/ 10 = 113789.5

Since the measurements were done for pure elements, the effect of absorption edges (self-absorption) on the background continuum is not expected to be significant. For each of the elements examined the energy windows over which integration was performed were those suggested by the DTSA software for the specified detector resolution. For the K-

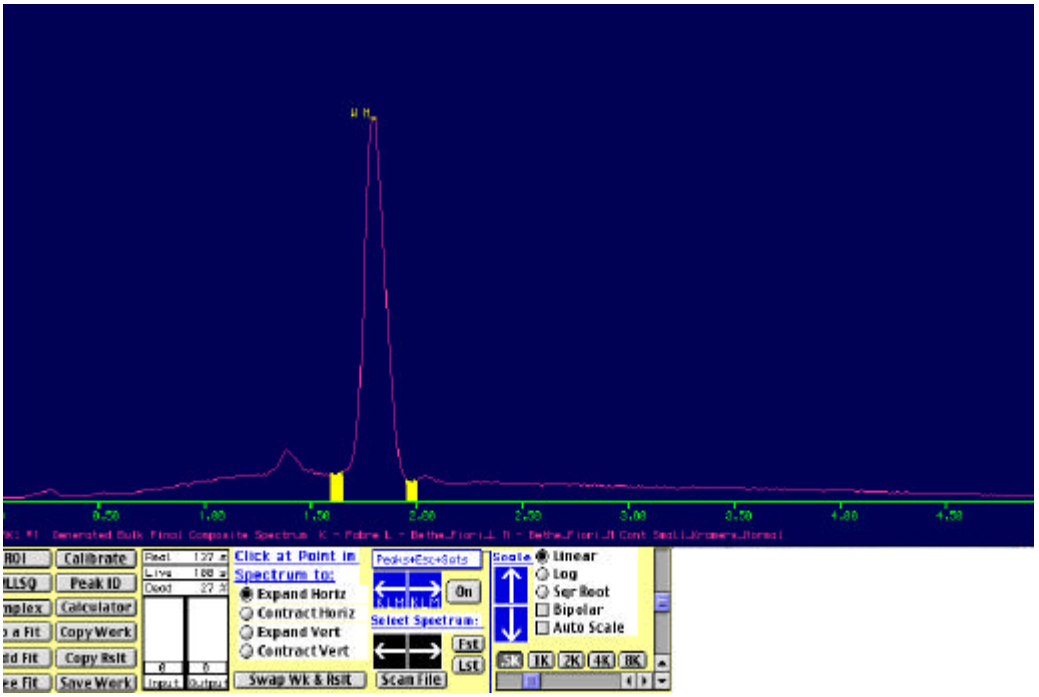

Figure 3.3. Linear Back-ground subtraction method.

lines this window included only the Ka contribution; for the L-lines the major component in the window was La_1 lines; and for the M-lines the major component was Ma_1 lines.

3.5.2 Count rate variation results

Since the live time correction is variable, depending on the count rate, one method of checking its accuracy was to check and see if the yield (which is on a per-electron basis) was independent of the beam current. There was essentially no variation in the yield determination at various count rates in spite of the variable live time correction. Figure (3.4) shows a typical experimental curve of X-ray count rate in units of photons per picoampere of current per second as a function of beam energy. To avoid clutter only few representative values are plotted, but the overall form of the count rate is the same for every element regardless of the shell type.

At energies just above the critical energy for the line the count rate is very low but it rises rapidly as the overvoltage increases and by 20 keV it is typically between 1 and 10 photons pA^{-1} s^{-1}. The absolute magnitude of the counts depends on the collection efficiency of the EDS detector employed, and so is specific to a particular electron beam column and analyzer, but the shape of the curve is dependent only on the details of the generation and subsequent escape of fluorescent X-rays from the target[2]. For analytical purposes, the generation efficiency will be plotted as a function of the overvoltage $U = E / E_{crit}$ (where E is the electron beam energy and E_{crit} is the critical excitation energy for the line).

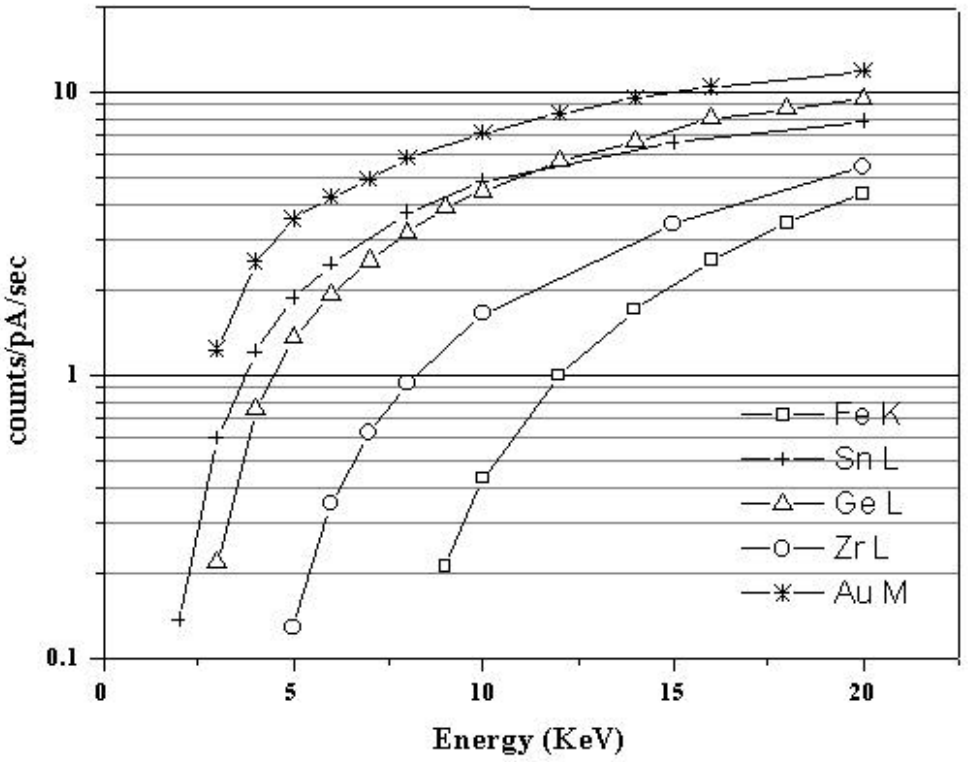

Figure 3.4 Variation of count rate with beam energy for selected K-, L-, M- lines

3.6 Data Analysis

Collected data were first background-subtracted as described above and illustrated in figure 3.3. Conversion of the number of measured counts per second (N_m) to the yield ($N_k/4?$), expressed in photons /incident electron /steradian, was then performed by use of equation 3.1

$$\frac{N_k}{4p} = \frac{N_m}{f(c)\Omega Dic} \tag{3.1}$$

where

$f(c)$ = absorption factor (Heinrich's value)[61]

O = solid angle subtended by the detector

D = detector absorption correction (for window, contact, and dead layer)

i = measured beam current

c = conversion from measured current to electrons/second.

3.6.1 Absorption correction

Following Green & Cosslett (1968) and Lifshin *et al.*(1980), let the number of X-ray quanta per sterad per incident electron observed at an angle ? to the surface be N(?)/4p

and let the number of quanta generated per sterad per incident electron within the target be N/4p. Then using the notation of Castaing & Descamps[62]

$$N(?)/4p = f(\chi).N/4p \qquad (3.2)$$

where $f(\chi)$ is the correction factor for self-absorption in the sample of the generated X-rays, χ is $(\mu/?)$ cosec? and $(\mu/?)$ is the mass absorption coefficient of the target material for a given characteristic line. At the take-off angle of $\theta = 35^{o}$ used for these measurements the $f(\chi)$ correction for self-absorption is generally not a major factor with $f(\chi)$ typically >0.95. For the analysis performed here the values of the mass absorption coefficients were taken from the tables in Goldstein *et al.*[7], which are based on the data sets prepared by Heinrich *et al* at NIST. The appropriate values of $f(\chi)$ were then computed from a Monte Carlo simulation (for example gold M-line absorption correction in figure 3.5). Because the samples were not cleaned in'situ and the surface is contaminated, allowance is made by including the effect of a carbon contaminant layer (~1nm) on the result for the take-off angle of $\theta = 35^{o}$ [63]

3.6.2 Detector Quantum Efficiency

The observed count rate is related to N(?) by the efficiency ? of the EDS detector which depends in turn on the solid angle subtended by the detector at the specimen, and by the transmission efficiency of the window in front of the detector diode.

The efficiency of a detector is specified in terms of its detective quantum efficiency (DQE) defined from the relationship[64]

$$DQE = (S/N)^2_{exp} / (S/N)^2_{theory} \qquad (3.3)$$

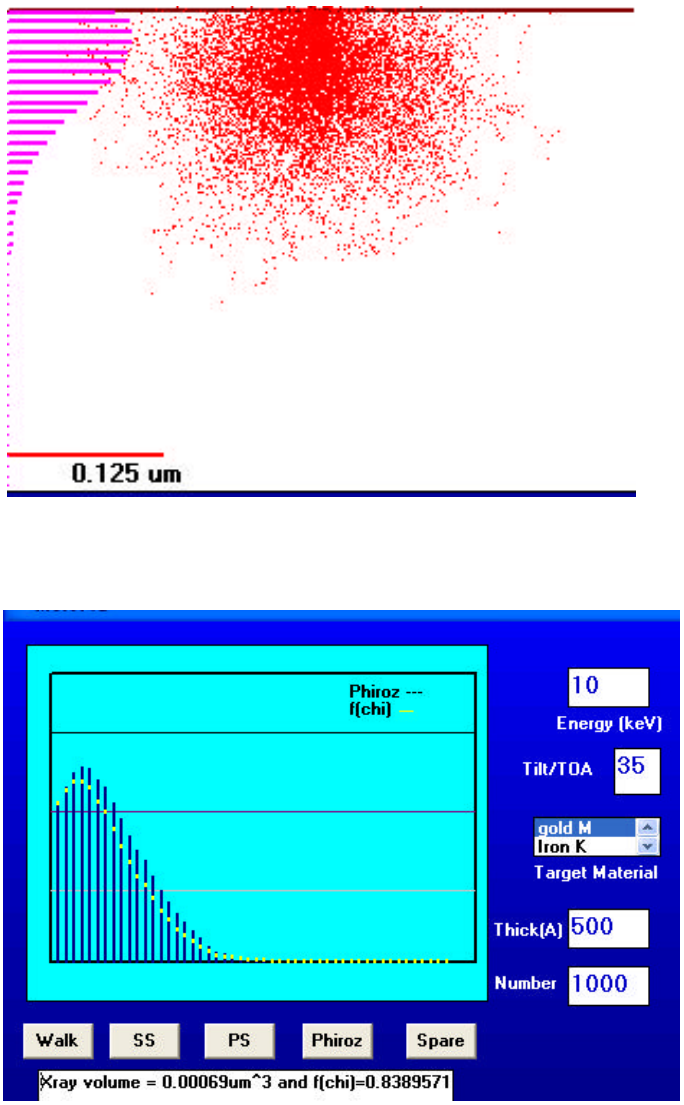

Figure 3.5 Monte-Carlo simulation of f(χ) correction for Au M-line

where $(S/N)_{exp}$ is the experimentally obtained signal-to-noise ratio (SNR) from a detector, and $(S/N)_{theory}$ is the predicted SNR from a perfect detector under the same conditions. The DQE is thus always less than unity and is a measure of how efficiently the detector makes use of the radiation reaching it.

To find the DQE of an energy-dispersive x-ray (EDS) detector, the goal is to be able to deduce the geometric collection efficiency of the detector, so the measurement was done at an x-ray energy where the quantum efficiency of the detector diode itself is unity and

where the transmission of the window in front of the detector is also unity. Both of these conditions can be satisfied for all detectors by performing the measurement at the copper K-line (8.0keV). Simulations performed using the NIST-NIH program DTSA show that, for normal incidence on a pure copper target at a beam energy of 20keV, the emitted flux of Cu K-line radiation is constant to much better than 1% for any take-off angle > about 5[?]. The emission therefore closely approximates an ideal hemispherical pattern and experimental measurements can then be performed for any detector geometry (azimuthal position and take-off angle) without changes to the form of the calculation.

The geometric efficiency term (which depends only on the solid angle and so is energy independent) was calculated both by direct estimation from the geometry of the detector collimator and diode and by measuring the detector quantum efficiency (DQE) of the detector which was obtained by comparing the measured yield for the Cu Kα line at 18 keV with an average of published values for the efficiency of Cu Kα production at an overvoltage ratio U=2 (18 keV).These measurements give a value of 0.003[65] (figure 3.6).

These conditions were used because the detection efficiency of Cu Kα line at U=2 is

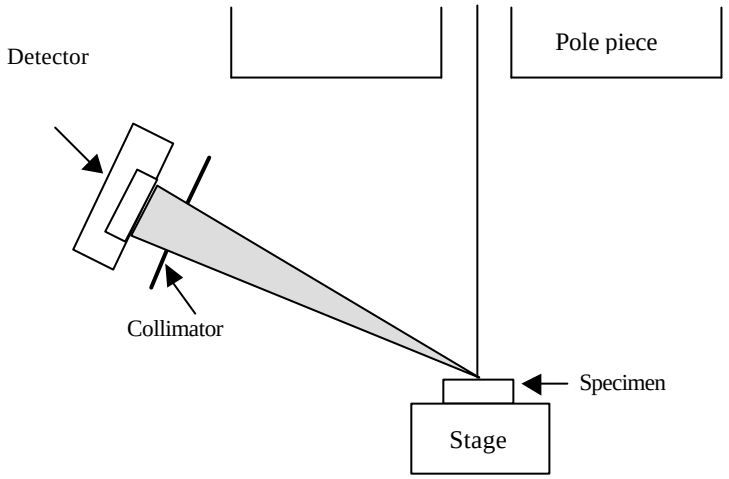

Figure 3.6 Solid angle of x-ray collection from the point of view of the specimen (dark shading)

almost unity due to negligible absorption in the detector window and there are several independent sets of data for the generation efficiency of Cu K lines at U=2. Errors in the geometrical efficiency term will not effect the relative yield efficiencies found for different elements but will change their absolute magnitude.

3.6.3 Window transmission correction

The radiation emitted from the specimen must pass through several layers of "window" material before it arrives in the "active" part of the detector. The nominal purpose of the first window material is to protect the cooled detector chip from the relatively poor vacuum in the specimen chamber which can be high in water vapor and organic components because of frequent exchanges of the specimen. It is very important that these components do not condense on the cooled detector. Even with a protective window, ice will build up, over a period of time, which will absorb lower energy x-rays. Modern detectors have special heaters to remove this ice buildup, some of which actually originates from the detector assembly and cryostat at the time of manufacture. This problem can be overcome by the use of high vacuum construction practices. Since many modern scanning and transmission electron microscopes themselves are ultra-high vacuum devices, the purpose of the window is actually to protect the microscope vacuum from that of the detector[66].

The protective window materials are constructed of thin films on a support grid having approximately 85% open space. Low energy x-rays, such as oxygen or carbon, will only pass through the un-backed portions of the film, while more energetic x-rays (>8 keV) can pass both through the film and the support grid. The grid is usually pure silicon or a

metal such as nickel and the window materials are either boron nitride, silicon nitride, diamond, or are polymeric. Since thin films of these materials are transparent and the detector is also sensitive to visible light, it is either necessary to eliminate possible light sources or to apply an optically opaque layer to the protective window. Light sources include microscope illumination systems, viewing ports, and light leaks; however, specimen cathodoluminescence is rarely intense enough to cause a serious problem. The second window layer is an electrical contact (about 10-20 nm and usually gold). Gold has been observed to form "islands" during the evaporation process and hence is not uniform in thickness. The third window layer consists of inactive p-type silicon extending 100-200 nm or less into the detector. This layer is also not uniform and is often called the "dead layer" or "silicon dead zone". The combined effect of these Au and Si layers is often overlooked. In reality, their effect is as great, or greater, than that of any of the new "thin" window materials.

During passage of x-rays through all of the window layers, absorption occurs. It is important to recall that photoelectric absorption refers to a process in which x-rays are diminished in number, but not in energy, thus the energies of the observed spectral lines are not altered by the effects. Absorption by the gold and silicon layers is much less significant because of the small mass thickness of these layers. However, a noticeable change in the x-ray continuum is observed at the absorption edge of silicon and to a lesser degree at gold. Just above the energy of the absorption edge, the mass absorption coefficient increases abruptly, resulting in a decrease in the measured continuum X-radiation. The height of the resulting step is an indication of the thickness of the layer. Note that the action of the broadening effect of the detection process causes the

absorption edge, which in reality is a sharp change of absorption over a range of about 1 eV, to be smeared over a much broader range, typically 100 eV for the silicon absorption edge.

The window transmission, which depends on the energy of the X-ray line, was computed by making a best fit to an experimental carbon (Highly Ordered Pyrolitic Graphite) continuum spectrum by iteratively refining the parameters defining the detector like window material (eg., Au layer, dead layer, Al, ice, etc.) and thickness by using the DTSA spectrum simulation tool over the energy range 500eV to 20keV. Errors in the computed window absorption will affect both the relative values between different elements and the absolute magnitudes. However, because the detector window is of the atmospheric thin window (ATW) type the window transmission efficiency exceeds 85% for almost all elements and as a result absorption will not to be a significant problem[2]. The efficiency of the detector as a function of photon energy is shown in figure 3.7.

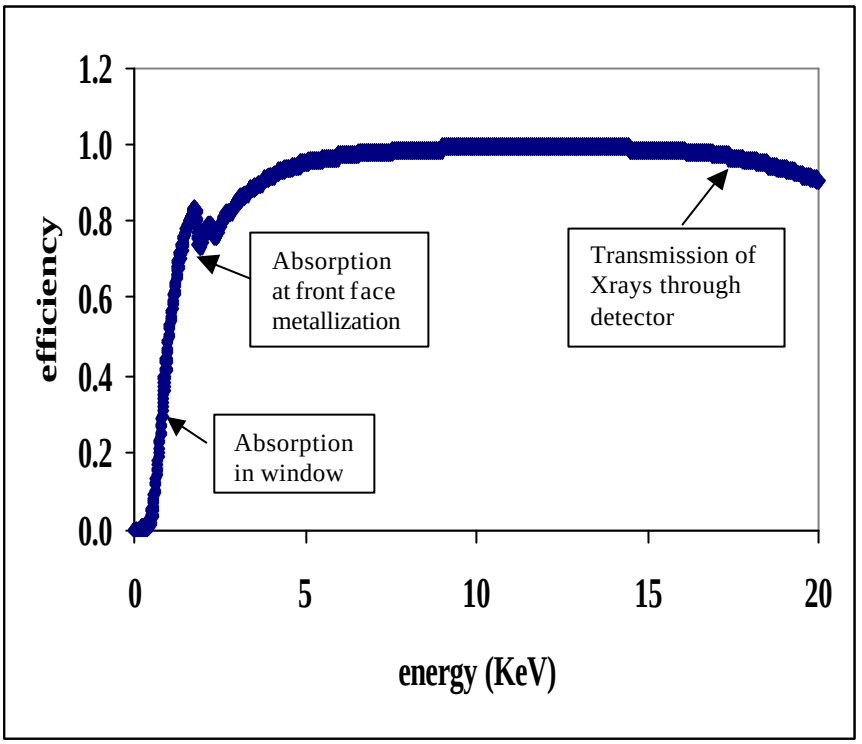

Figure 3.7. Window transmission efficiency curve

CHAPTER 4

4.1 Discussion

By knowing the efficiency of the EDS detector and the necessary *f*(?) correction, the measured yield in counts per picoampere per second were corrected to give N / 4? – the generation efficiency of X-rays within the target in photons per steradian per electron. As first shown by Compton & Allison[67], the magnitude of N / 4? for *K* lines has a functional variation with the overvoltage U of the form

$$N / 4? = N_0 / 4? \times (U-1)^n = A (U-1)^n \quad (4.1)$$

The measured data are therefore plotted (figure 4.1) on the logarithmic axes as a function of (U-1). It can be seen that the agreement between the proposed power law behavior and the experimental data is generally good. For the eight *K* lines measured (Si, Sc, Ti, V, Cr, Fe, Co and Cu), the magnitude of the exponent 'n' determined by a fitting procedure varies from 1.21 for Si to 1.83 for Fe to 2.0 for Cu. These values are in good agreement with those quoted by other authors[2]. The efficiency pre-factor A in equation (4.1) varies from 6.0×10^{-5} for Si to 1.0×10^{-4} for Cu.

The efficiency data for the Sc, Ti, V, Cr, Fe, Co, Cu, Ge, Zr, Sn, Sb, Hf, W, Ir, Pt, Au and Pb *L*- lines calculated from the measured count rate data as discussed above were also plotted against the (U-1) on the logarithmic axes. The data for selected elements is shown

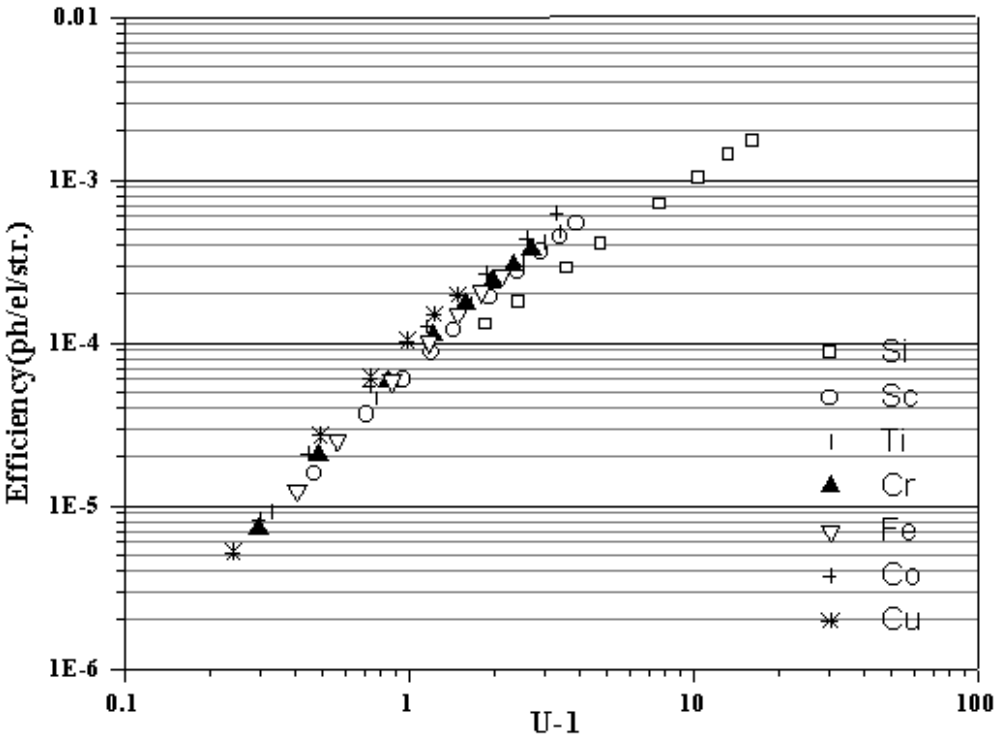

Figure 4.1. Variation of absolute X-ray generation efficiency (photons / steradian / electron) as a function of (U-1) for the K-lines of Si, Sc, Ti, Cr, Fe, Co and Cu.

in figure 4.2 to avoid excessive overlap of plots. It can be seen that the Compton and Allison equation also applies to the *L* data. The value of the corresponding pre-factor A varies from 5.0×10^{-7} for Sc to 9.0×10^{-5} for Ir and again curves generally increase with atomic number. The value of the exponent 'n' also rises with atomic number and shows a wider range than for the *K* lines varying from 0.33 for Ti to as high as 2.49 for Au. Figure 4.3 shows the variation of X-ray generation efficiency for the M-lines of Hf, W, Ir, Pt, Au and Pb plotted as a function of (U-1) as before. The shape of the generation efficiency profile when plotted on the logarithmic axes again agrees well with the Compton & Allison equation. For *M* shells, 'n' varies from 0.85 for Hf to 1.31 for Pb ranging intermediate between the *K* and *L* values where A varies from 8.0×10^{-5} for W to 3.0×10^{-4} for Ir.

Table 4.1 shows the pre-factor and exponent values of X-ray yields. Note that the efficiency at U = 2 is equal to A. The exponent values of *L* and *M* lines quoted are those determined at higher overvoltages (U>2) because the statistics of data collection at low overvoltages were not good enough to be representative of the behavior of the pure element. Figure 4.4 shows the variation of the generation pre-constant A in the efficiency equation as a function of atomic number. It is interesting to note that A is higher for *K* lines and *M*-lines than for *L* lines. This result is not immediately obvious from an examination of cross-section and fluorescent yield data. The dependence of generation efficiency on the overvoltage as well as atomic number is shown in figure 4.5. As can be seen from the plot, the X-ray yield increases with both overvoltage and atomic number. Also at higher overvoltages, the generation efficiency of *K* lines is greater than *L* lines

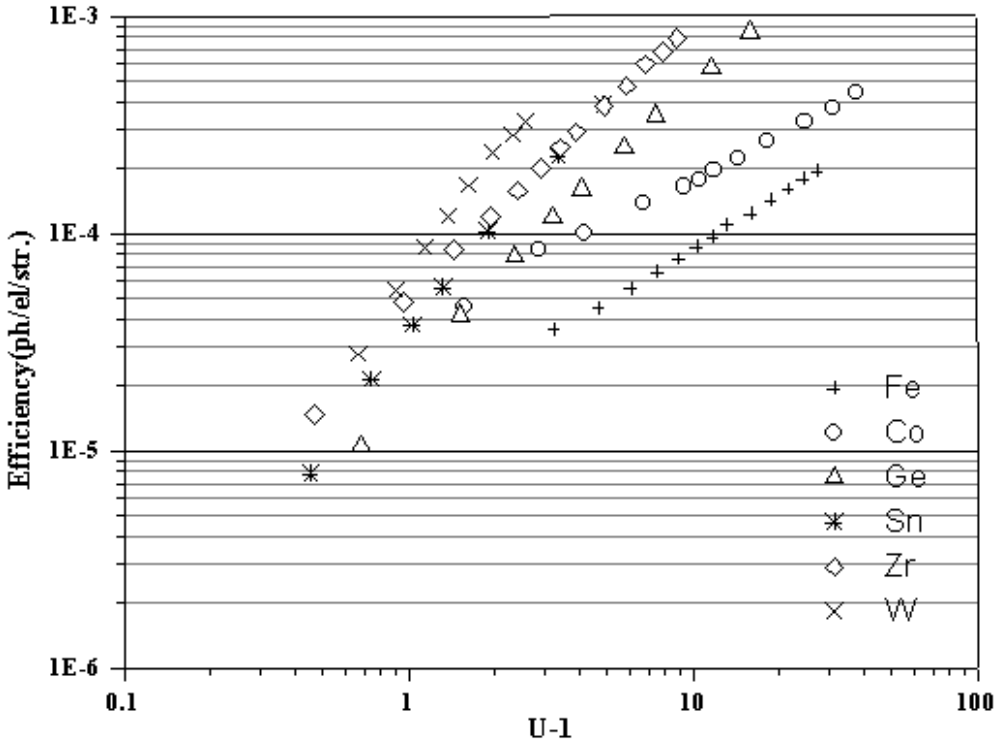

Figure 4.2. Variation of absolute X-ray generation efficiency (photons/ steradian/ electron) as a function of (U-1) for the *L* lines of Fe, Co, Ge, Sn, Zr and W

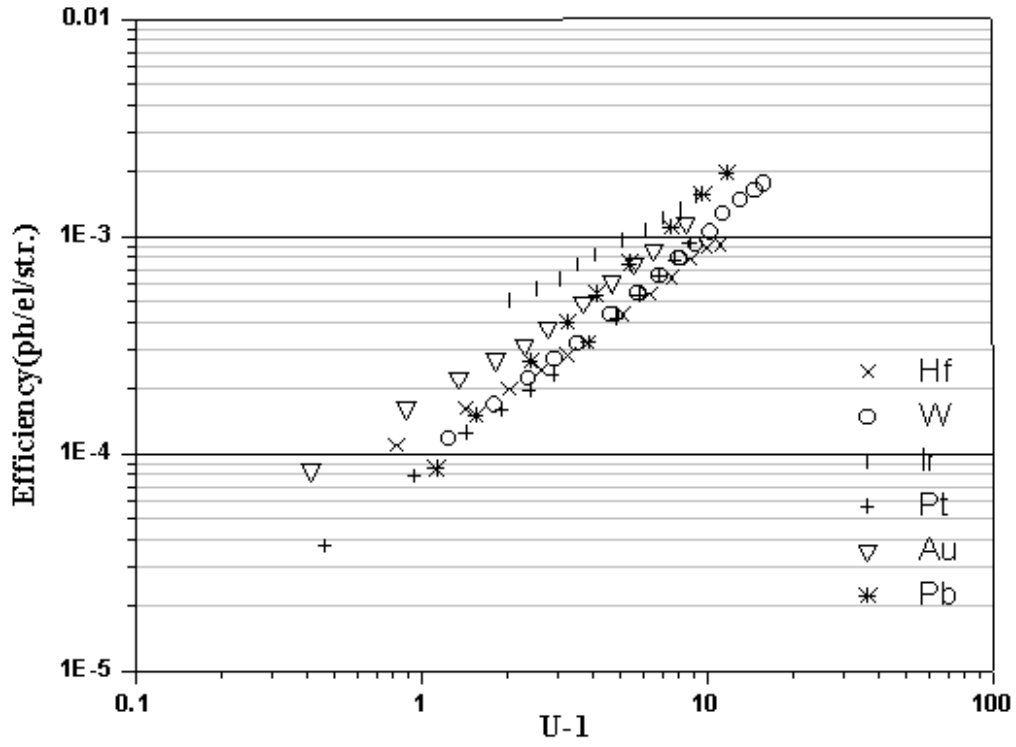

Figure 4.3 Variation of absolute X-ray generation efficiency (photons/ steradian/ electron) as a function of (U-1) for the *M* lines of Hf, W, Ir, Pt, Au and Pb

Table 4.1 Efficiency and exponent values of X-ray yields**.**

Element	Shell	Exponent 'n'	Pre-factor 'A' (efficiency at U=2)
Si	K	1.21	6.11E-05
Sc	K	1.65	6.18E-05
	L	0.97	4.82E-07
Ti	K	1.70	6.63E-05
	L	0.33	1.59E-05
V	K	1.65	7.78E-05
	L	0.63	1.04E-05
Cr	K	1.77	7.12E-05
	L	0.65	1.61E-05
Fe	K	1.83	7.04E-05
	L	0.80	1.33E-05
Co	K	1.77	8.34E-05
	L	0.68	3.68E-05
Cu	K	2.00	1.00E-04
	L	0.78	1.13E-04
Ge	L	1.36	2.19E-05
Zr	L	1.33	4.72E-05
Sn	L	1.62	3.30E-05
Sb	L	1.32	4.17E-05
Hf	L	2.06	6.47E-05
	M	0.86	1.13E-04
W	L	1.82	6.39E-05
	M	1.11	8.03E-05
Ir	L	2.06	9.46E-05
	M	0.73	2.90E-04
Pt	L	2.44	6.19E-05
	M	1.07	8.07E-05
Au	L	2.49	7.57E-05
	M	0.85	1.70E-04
Pb	L	2.20	7.55E-05
	M	1.31	8.06E-05

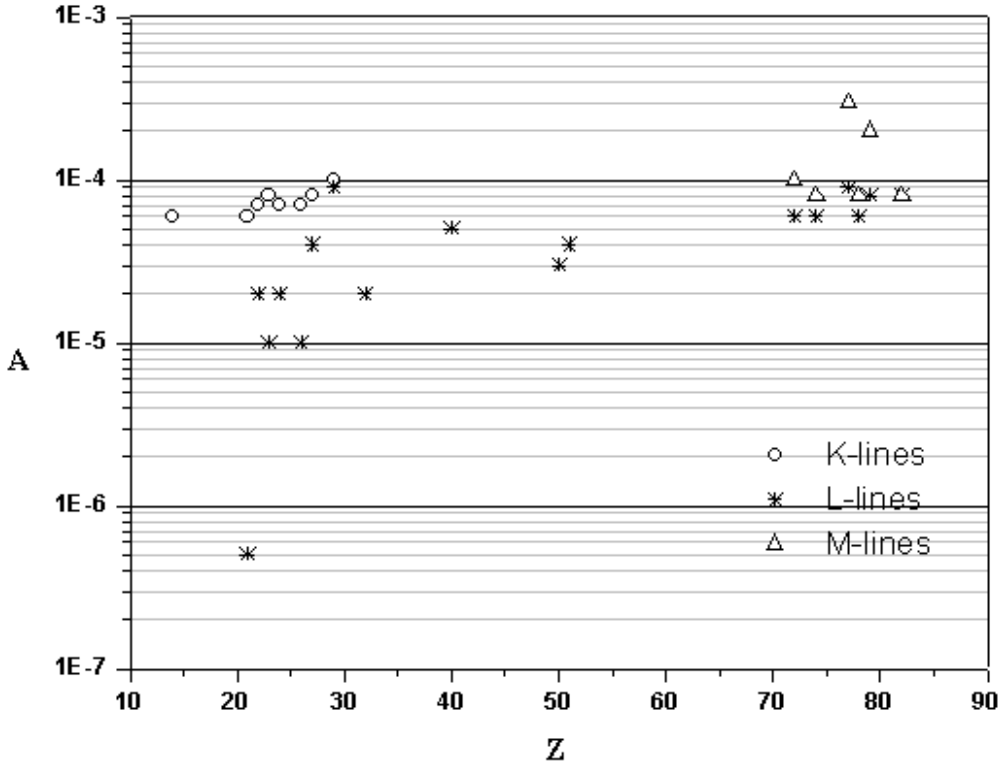

Figure 4.4 Variation of X-ray generation pre-constant 'A' as a function of atomic number

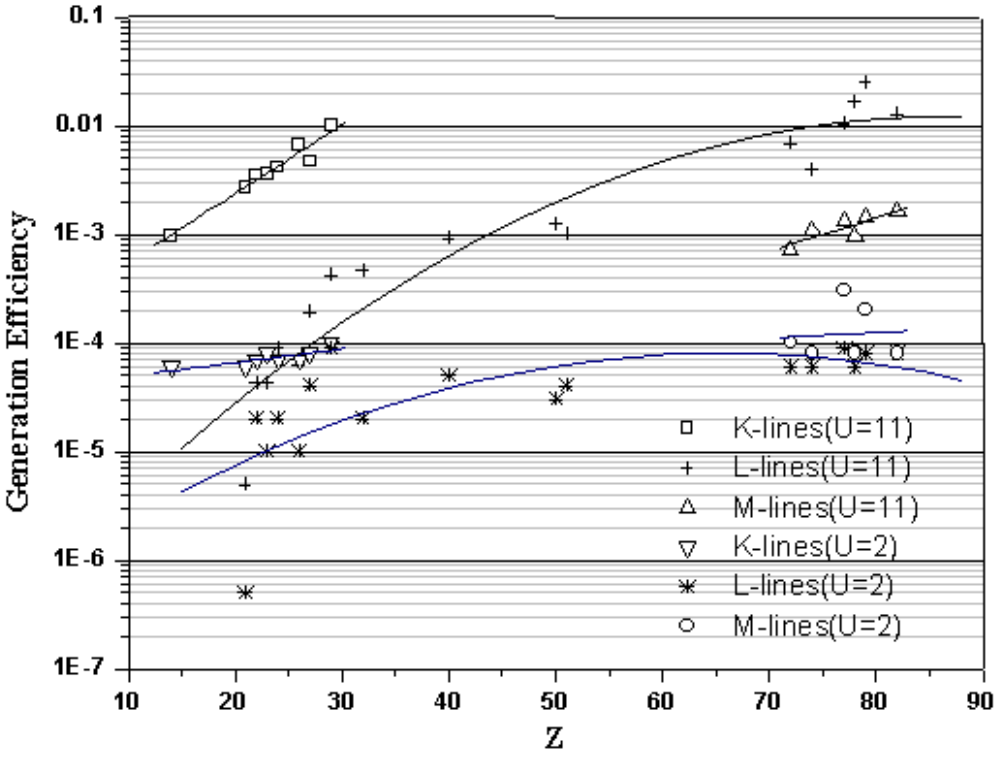

Figure 4.5 Variation of X-ray generation efficiency (photons/ steradian/ electron) as a function of overvoltage and atomic number

which are in turn greater than the *M* lines. But as the overvoltage drops to 2, i.e., (U-1) = 1, the generation of *M* lines become more efficient than that of *L* lines. Figure 4.6 shows the variation of exponent 'n' with atomic number. It can be seen that the slope of the curves decreases from *K* shell to *L* shell to *M* shell.

While theoretical cross-section data may not be accurate enough to predict an absolute yield efficiency, it is instructive to compare relative yields from these models against a standard such as Cu *K*a. To understand the behavior it is necessary to compare experimental and theoretical values. The comparison between the generation efficiency of *K*-lines at (U-1)=1 for the experiment and the simulated data using WINCASINO[68] and the Casnati , Brown-Powell and Gryzinsky cross-section models is shown in figure 4.7. The experimental data were corrected for the detector efficiency, solid angle and absorption while the simulated data is only corrected for absorption. This does not affect the relative trend of the profiles and it can be seen there is a monotonic variation of X-ray generation efficiency with atomic number for *K*- shells. Also all the three models seem to predict relative *K*-shell efficiency well within 5 percent error. Similarly, data was plotted for *L*-lines in figure 4.8 and here also a monotonic variation of X-ray generation efficiency with atomic number can be seen although the models considered are off by 30 percent error.

In figure 4.9, comparison between experimental and simulated data for *M*-lines is shown and it is interesting to note that the experimental curve follows the Casnati model within 30 percent error. The errors in the experimental data of *L*- and *M*-lines could be due to poor statistics at low overvoltages and peak overlap making the background correction

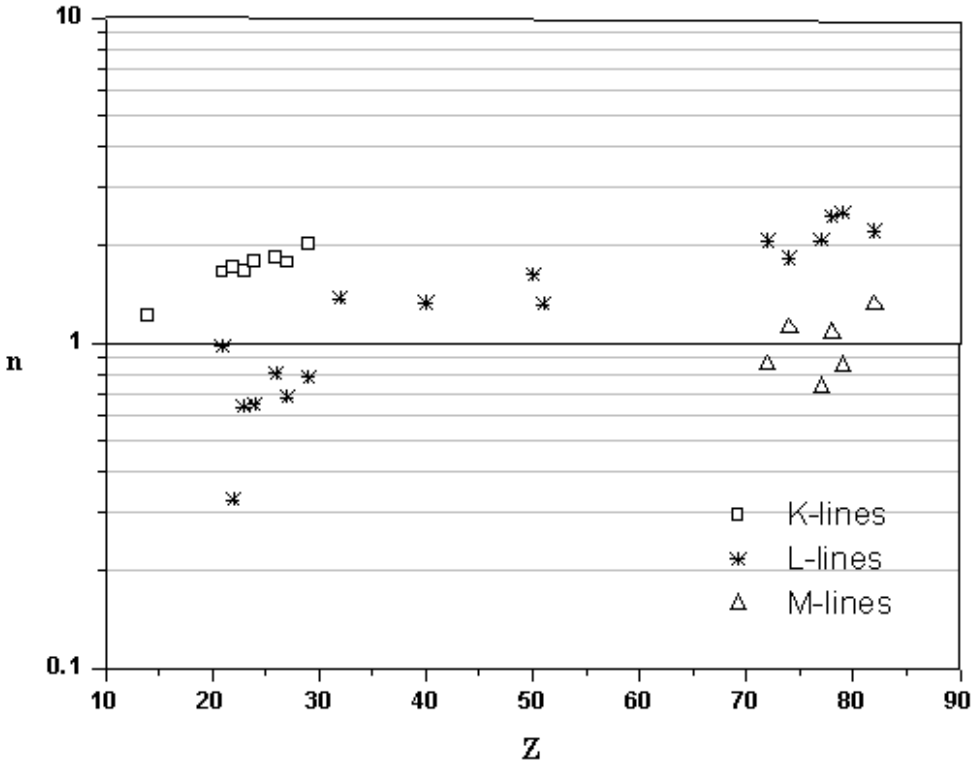

Figure 4.6 Variation of 'n' with atomic number

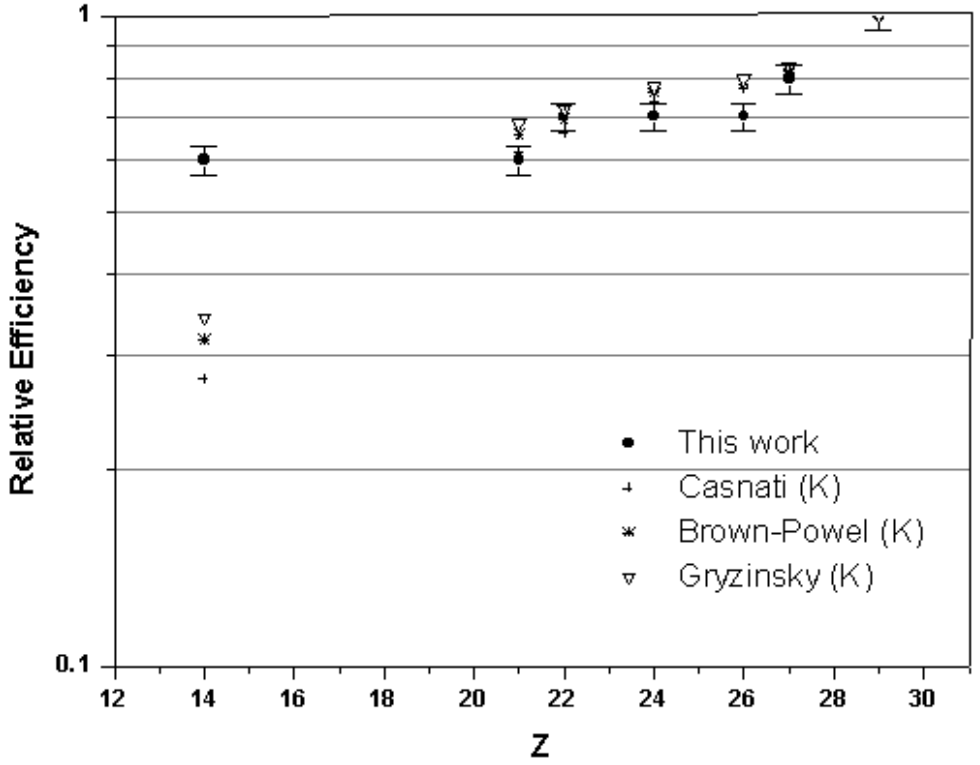

Figure 4.7 Comparison between experimental and simulated data for *K* line efficiency at U = 2

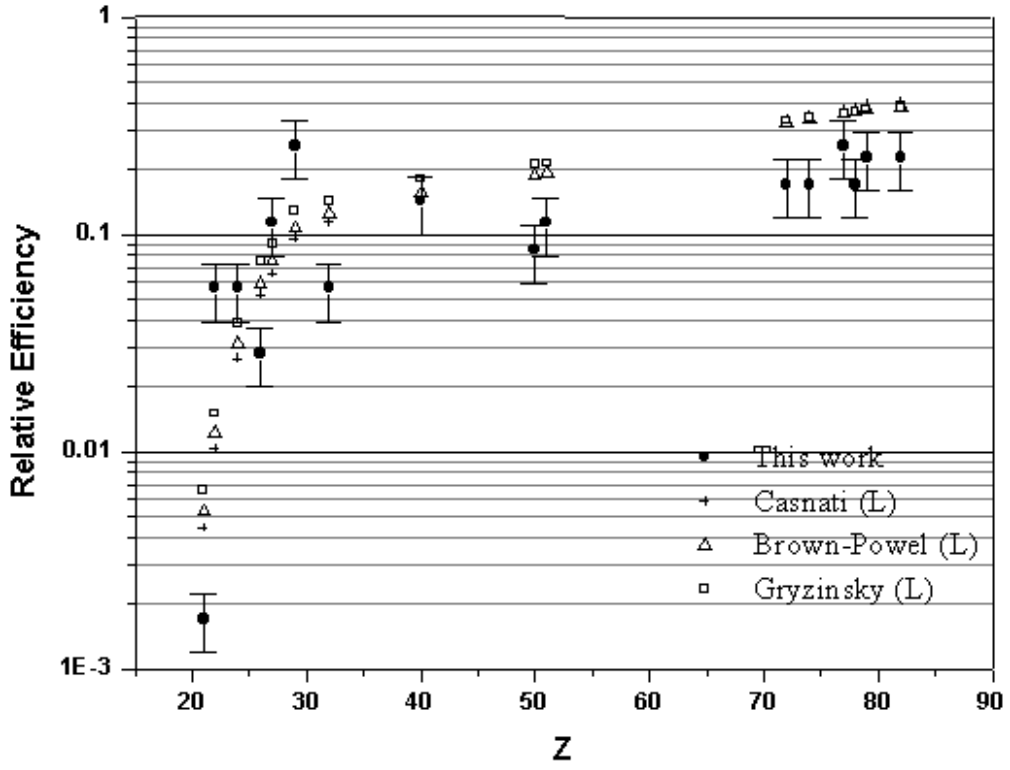

Figure 4.8 Comparison between experimental and simulated data for *L* line efficiency at U = 2

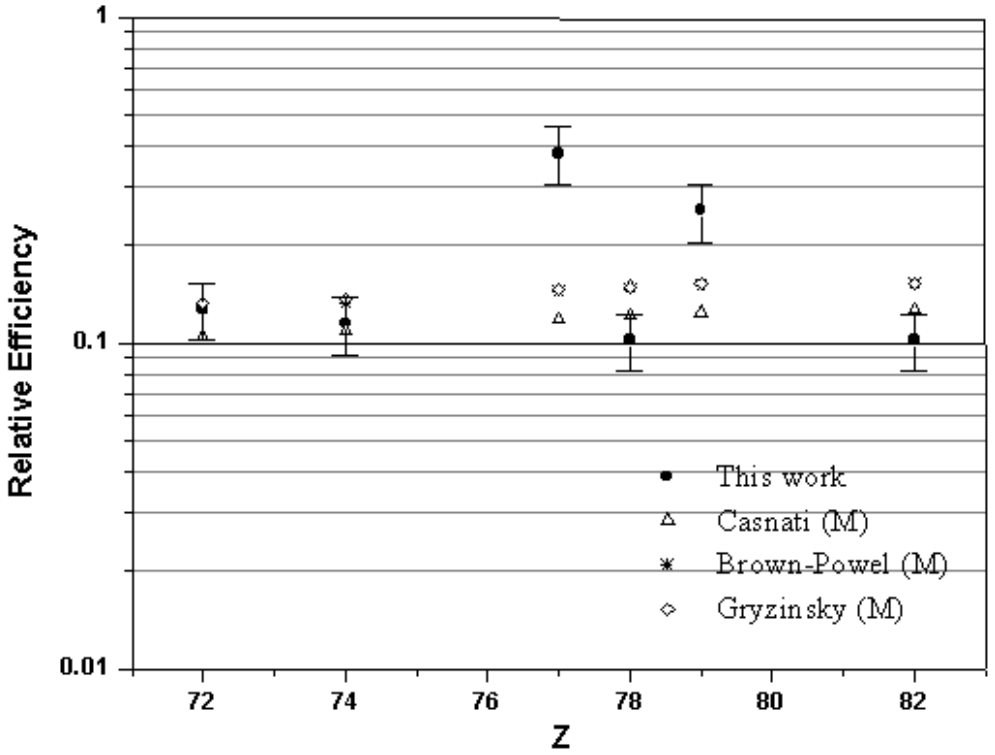

Figure 4.9 Comparison between experimental and simulated data for *M* line efficiency at U = 2

inaccurate. Also the discrepancies in mass absorption coefficient data used in $f(\chi)$ correction could add to the errors.

The comparison confirms that both the experimental and theoretical X-ray yield data has a simple functional variation with atomic number at a fixed overvoltage, unlike the complex variation of the ionization cross-section. The monotonic behavior of the efficiency, and of the 'A' and 'n' variables which describe it, implies that the data can be successfully parameterized. This makes it possible to predict efficiencies easily and accurately for any chosen energy. In addition this knowledge of efficiency can be employed to estimate cross-section for elements where no direct measurement is feasible. This requires a knowledge of the fluorescent yield and for *L*- and *M*- shells such data is scarce and unreliable because of the correction required to account for Coster-Kronig transitions, and in addition ? may vary with bonding. However, as shown by Eades et al. (to be published) fluorescent yields of *K*, *L* and *M* lines fall on a universal curve when plotted against their excitation energy. Although a rigorous theoretical explanation is still missing for Eades hypothesis, it suggests that missing ? values for *L* and *M* lines can be estimated with good reliability. Comparing these values to the fitted generation efficiency then allow s to be derived as a starting point for further theoretical studies.

PART 2

Secondary Electron Spectroscopy

CHAPTER 5

5.1 Background

When the surface of a solid is bombarded with charged particles of sufficient kinetic energy, emission of electrons by the solid may be observed. This phenomenon of secondary electron emission was discovered by Austin and Starke in 1902 in a study of the reflection of electrons by metals; they observed that under certain circumstances more electrons were emitted than were incident, indicating that the bombarding primary electrons liberate electrons from the solid[69].

When a beam of primary electrons strikes the surface of a solid, a certain fraction is elastically reflected and the remainder penetrates into the solid. The primaries that enter the solid will lose energy by exciting lattice electrons into higher energy levels. The latter may then move toward the surface and a certain fraction will escape from the solid as secondaries. It is also possible that a primary electron, which has lost part of its energy inside the solid, returns to and escapes from the surface as a result of Rutherford scattering; such electrons are called inelastically reflected primaries. The electrons leaving the surface are therefore distinguished between three categories[70]:

a) Elastically reflected primaries

b) Inelastically reflected primaries

c) “True” secondaries

This is better explained by reference to figure 5.1, which shows a typical energy distribution of the electrons emitted from a metal surface. The electrons in region III correspond to elastically scattered electrons and electrons which have collided with phonons losing energy of the order of a few hundredths of an eV. Electrons which lost more energy appear in region II. This region is characterized by certain peaks corresponding to inelastic collisions of the incident (primary) electron with plasmons (collective oscillations of the electrons) and with other electrons. The energy of these peaks is fixed relative to the primary energy (they lie between 2 and 50 eV below it) and is determined by the excitation energy of plasmons and of interband electronic transactions. Region I consists of the true secondary electrons which are generated by the cascade process[71]. Because of a series of (random) collisions that (presumably) occur between the initial one (involving the incident electron) and the final event, i.e. the escape of the secondary electron from the metal, the latter retains very little information about the incident electron. Consequently the shape of the energy and angular distribution of the emitted secondary electrons should be practically independent of the energy E_p and of the direction of the incident electron beam, provided E_p is sufficiently large. It is impossible to draw a sharp distinction between true secondaries and inelastically reflected electrons; in fact, from figure 5.1 it is evident that the flat region of the curve consists of mixture of the two categories. Somewhat arbitrarily, the term "true secondaries" usually refers to all those electrons with an energy below about 50 eV. Following their discovery at the beginning of the twentieth century SE were the subject of intense experimental study for a period of 20 years or more from the early 1930s,

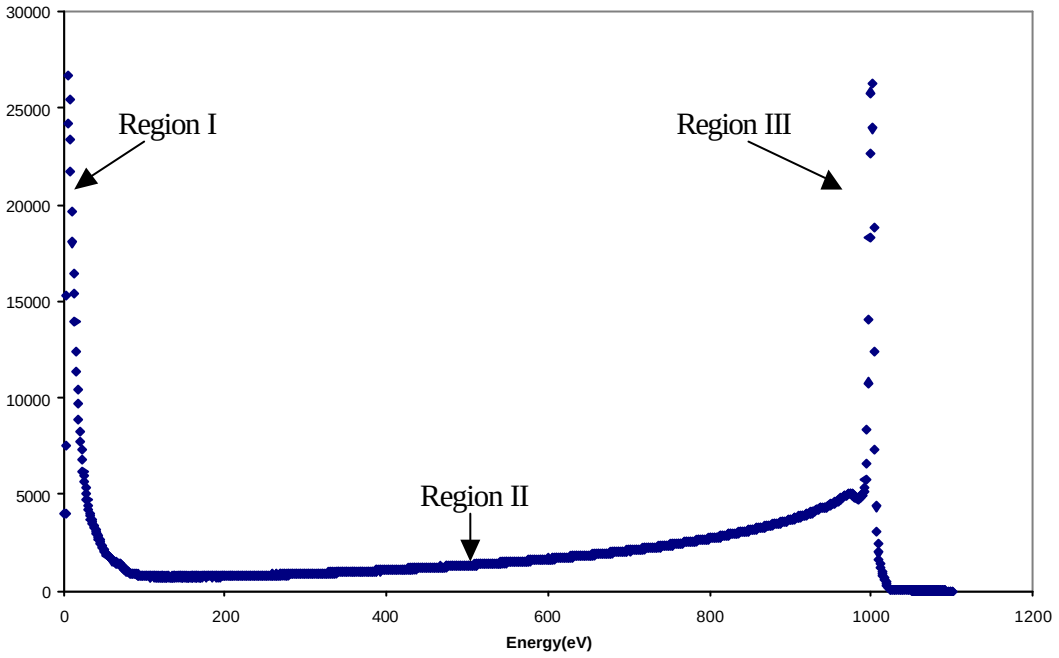

Figure 5.1 Electron energy distribution for gold at 1 keV

resulting in the publication of half a dozen books (see for example Bruining, 1942) on the topic.SE emission has been reviewed by Bruining (1954)[72], Kollath (1956)[73], Ardenne (1956)[74], Jonker (1957)[75], Dekker (1958)[76], Hachenberg and Brauer (1959)[77], Whetten (1961)[78], and Bronshtein and Fraiman (1969)[79]. Experimental and theoretical work is described by Kanter (1961)[80], Jahrreiss (1965)[81], Wittry (1966)[82], Mayer and Holzl (1966)[83], Seiler (1967, 1968)[84, 85], Applet (1968)[86], Simon and William (1968)[87], Seah (1969)[88], Drescher *et. al.* (1970)[89], Shimizu and Murata (1971)[90], Kanaya and Kawakatsu (1972)[91], Murata (1973)[92], Shimizu (1974)[93], Fitting (1974, 1980)[94,95], Willis and Feuerbach (1975)[96], Voreades (1976)[97], Pillon *et al.* (1976)[98], Chung and Everhart (1977)[99], Reimer and Drescher (1977)[100], Kanaya and Ono (1978)[101], Alig and Bloom (1978)[102], Ono and Kanaya (1979)[103], Ganachaud and Cailler (1979)[104], Chase *et al.* (1980)[105], Rosler and Brauer (1981)[106], Cailler *et al.*(1981)[107], Seiler (1983)[108], Halbritter (1982)[109] to name a few. This research effort did not, however, produce as much fundamental data as might have been expected because the usual goal of this early work was to demonstrate that the variation of the SE yield with incident electron energy followed a 'universal law' (Seiler, 1983)[108], and to find the parameters describing this profile. The advent of the scanning electron microscope (SEM), which relies on secondary electrons for its most popular mode of imaging, ensured continuing interest in the properties of SE although again most experimental work has been concentrated on the yield variation with energy because of its importance in understanding the charging behavior of insulating samples[110,111] . However, many users of SEM have begun to recognize that a knowledge of the energy spectrum of the secondaries would be of value

in interpreting images and in designing more efficient and contrast specific detector systems[112, 113, 114].

Unfortunately although there are many papers that refer to SE spectroscopy (Whetten & Leponsky[115]; Modinos[71]; Keneko[116]; Sakai *et al*[113]) these are often of limited value for users of the SEM because the data have been recorded in an ultrahigh – vacuum (UHV) environment from clean sample surfaces. By contrast, most SEMs only provide a relatively poor vacuum in the specimen chamber, and so sample surfaces are invariably covered with films of hydrocarbon, oxide and water. The maximum depth from which secondary electrons can escape to the vacuum is generally taken to be the order of 5-10nm (Seiler[108]; Alig & Bloom[102]; Grais & Bastawros[117]). This distance is of the same scale as the expected thickness of the contaminating surface layers, and thus it is usual to assume that the spectrum of secondary electrons measured under such conditions would be quite different to that measured from a clean sample, and might indeed be representative only of the surface films themselves. The purpose of this study is to test whether or not that assertion is correct, and to determine the nature, and the possible utility, of the SE spectra that might be encountered in an SEM environment.

5.2 Experimental Procedure

Secondary electron spectra were recorded in a Schottky field emission gun PHI model 680 scanning auger nanoprobe (SAN) (Physical Electronics, Eden Prairie, MN, U.S.A.), equipped with a cylindrical mirror analyzer (CMA) with an energy resolution better than

1 eV. Although the specimen chamber vacuum of the PHI SAN can approach 10^{-7} Pa no attempt was made to approach that level during these experiments. A total of 32 different materials were examined, the majority of these being taken from a multi-element standard block (Energy Beam Sciences, Agawam, MA, U.S.A.) designed for X-ray microanalysis. The surface of the standard was prepared by mechanical polishing so as to produce a macroscopically flat, and microscopically smooth, surface. Regardless of their origin or history all samples are examined 'as received' with no additional cleaning of any kind. For comparative purposes, however, some samples were also ion sputter cleaned *in situ* in the SAM after the initial examination and then re-measured in a clean condition.

The spectra were recorded digitally using the software of the PHI 680, which was operated in the range 1-10 keV with beam currents of the order of 10nA. The dwell time per channel was about 0.1 s and six to eight were acquired and then averaged to yield the final spectrum. Because the detector responds to both the energy and the number of electrons received the spectrum recorded represents the quantity *E.N(E)*, where *N(E)* is the number of electrons emitted within the 1 eV- wide acceptance energy window of the CMA at the energy *E*, as a function of *E*. The sample was oriented normal to the beam and to the entrance axis of the CMA, which accepts electrons over an angular range of 42 $\pm$ 6? integrated around the full 360? azimuth. The analyzer was operated at a resolution of 1 eV intervals from zero upto the incident beam energy (typically 1 or 3 keV). The kinetic energy E_{kin} of electron leaving a sample which has a work function ? is measured by the electrostatic energy analyzer as E'_{kin} (Oechsner, 1993)[118] where

$$E'_{kin} = E_{kin} + ? - ?_A \quad (5.1)$$

and $?_A$ is the 'analyzer work function' and a constant of the apparatus. The analyzer is initially calibrated, and $?_A$ is determined, from a reference copper sample adjusted so that the characteristic Auger edges occur at their correct energies. When measurements are made from specimens that have a different local work function the resultant shift in the spectrum is compensated by changing the bias *U* applied to the sample so that E'_{kin} is zero when E_{kin} is also zero. This occurs when $eU = ? - ?_A$ where *e* is the electronic charge. This ensures that Auger peaks always show at their expected energies, but masks the shifts in the onset energy of the true secondaries that occur as a result of work function variations[118]. The complete emission spectra in most cases displayed the expected Auger peaks from the material under observation, together with carbon, oxygen and sulphur peaks from the surface confirming the contaminated nature of these samples.

5.3 Results

5.3.1. From pure elements

Figure 5.2 shows the *E.N(E)* against E spectra recorded from ten elements – Al, Ag, Cr, Hf, Pd, Rh, Sb, Si, Sn and Zn – at 1 keV beam energy using the conditions described above. The beam current and calibration conditions were maintained constant through this series of measurements so the relative heights of the profiles are directly proportional to their SE yield coefficient at 1 keV. Although there is a definite generic shape to the

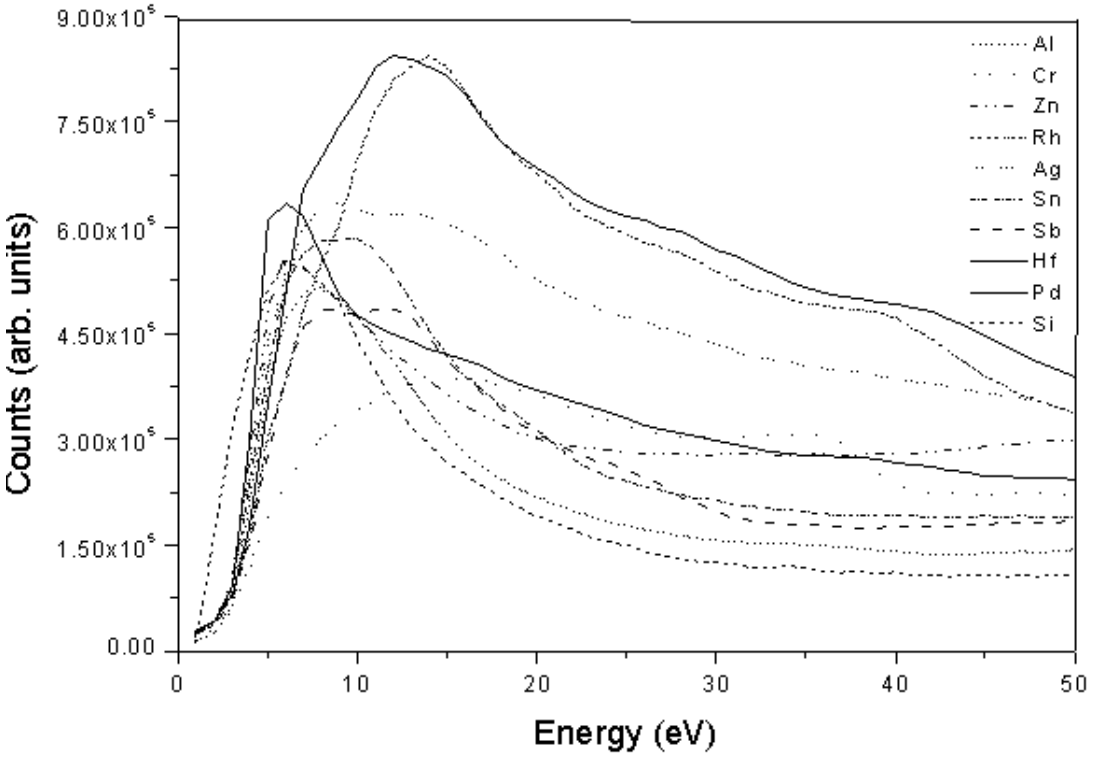

Figure 5.2. Composite plot of *E.N(E)* vs. *E* secondary electron spectra recorded from ten elements at an energy of 1 keV

spectra it is evident that there is a considerable degree of variation between them. In every case there is an initial rapid rise in the signal amplitude to a peak value. This peak is then followed by a region over which the signal again falls with increasing electron energy. For light elements, such as aluminum and silicon, the peak occurs at about 56 eV and is quite pronounced. For heavier elements the energy at which the peak signal amplitude is observed seems to rise, reaching 15 eV for Pd, and the peak becomes less well defined and broader. Beyond the peak position in the spectrum the signal amplitude falls rapidly for the low atomic number elements such as Al and Si, but more slowly for heavier elements such as Pd and Rh. In most cases the SE spectra were found to be quite reproducible, as demonstrated in figure 5.3, which compares data from randomly selected pieces of silicon wafer. The 'old' spectrum, recorded on a PHI 660 SAM, was taken 2 years before the 'new' data derived from the PHI 680 used for the majority of the work in this study. The spectra have been normalized to the same maximum height, and show very close agreement in their shape and profile. A comparison of data from other samples recorded at time intervals varying from a few months to a year or more also showed little or no change.

The form of the *E.N(E)* SE spectra were examined as a function of beam energy, as illustrated in figure 5.4, which compares silicon SE spectra recorded at 1, 1.3, 2 and 3 keV. The shape of each of the spectra is seen to be quite similar at all energies, but the magnitude of the yield is scaled in value by the steady fall in SE yield as the beam energy is increased. For all of the specimens used in this work it was confirmed that the form of the spectrum was, to a good approximation, independent of the incident beam energy.

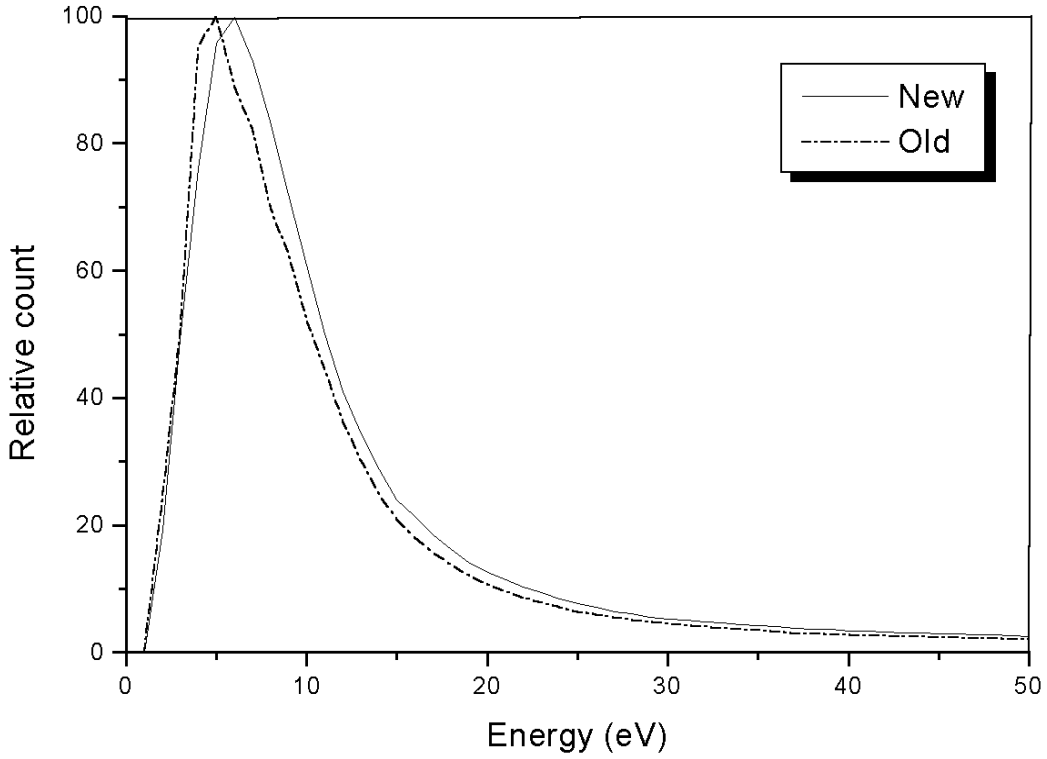

Figure 5.3. Comparison of *E.N(E)* spectra from two fragments of silicon wafer recorded on two different machines and 2 years apart

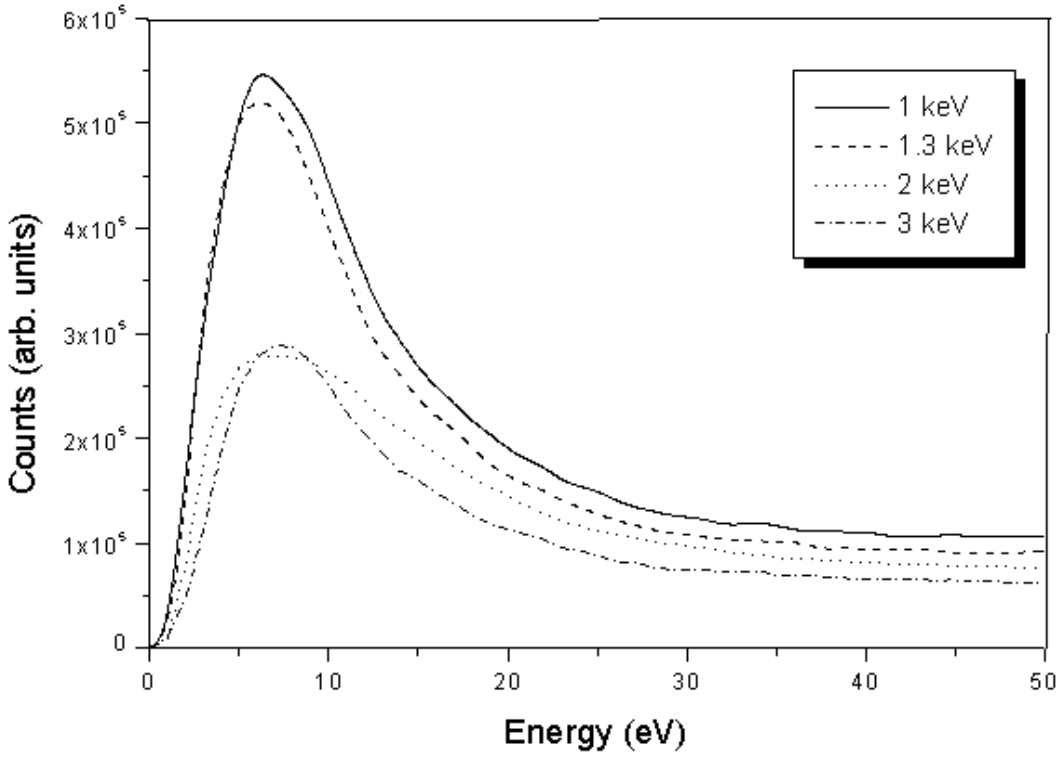

Figure 5.4. Variation of *E.N(E)* spectra from silicon as a function of incident beam energy from 1 to 3 keV

Figure 5.5 shows the same data as figure 5.2, but now replotted in the *N(E)* vs. E format. In this representation the similarities in the general appearance of the spectra from the ten elements are more evident, because each consists of a well-defined peak followed by a more or less rapid fall in intensity. In two cases (Pd, Rh) there is also evidence of a subsidiary shoulder, or minor peak, at a higher energy than the main peak. There are clearly differences in the energy at which the highest signal intensity occurs, and in the width of the peak, but these are less evident than the variations observed in the *E. N(E)* representation. When seeking to understand the processes that influence the details of SE imaging in the SEM the *N(E)* profile is clearly the more relevant form in which to present the data. However, for the purposes of discussion the *E.N(E)* spectrum is more convenient because it not only makes differences between spectra from various materials more evident, but it also compresses the dynamic range of the data, which allows the shape of the spectral profile to be more conveniently viewed across the full 50-eV window.

5.3.2 From compounds

For comparison, figure 5.6(a, b) show selected SE spectra, again obtained at 1 keV and under the same conditions as for the previous samples, from a group of compounds rather than pure elements. Four of the materials shown here are compound semiconductors – CdTe, GaAs, GaSb and lnP – and the fifth is the widely used polymeric resist material poly methyl methacrylate (PMMA). As before all of the data were recorded with constant gain calibration so the relative height of the profiles scales directly with the SE yield of the material. The *E.N(E)* spectra (figure 5.6a) look similar to the examples from elements

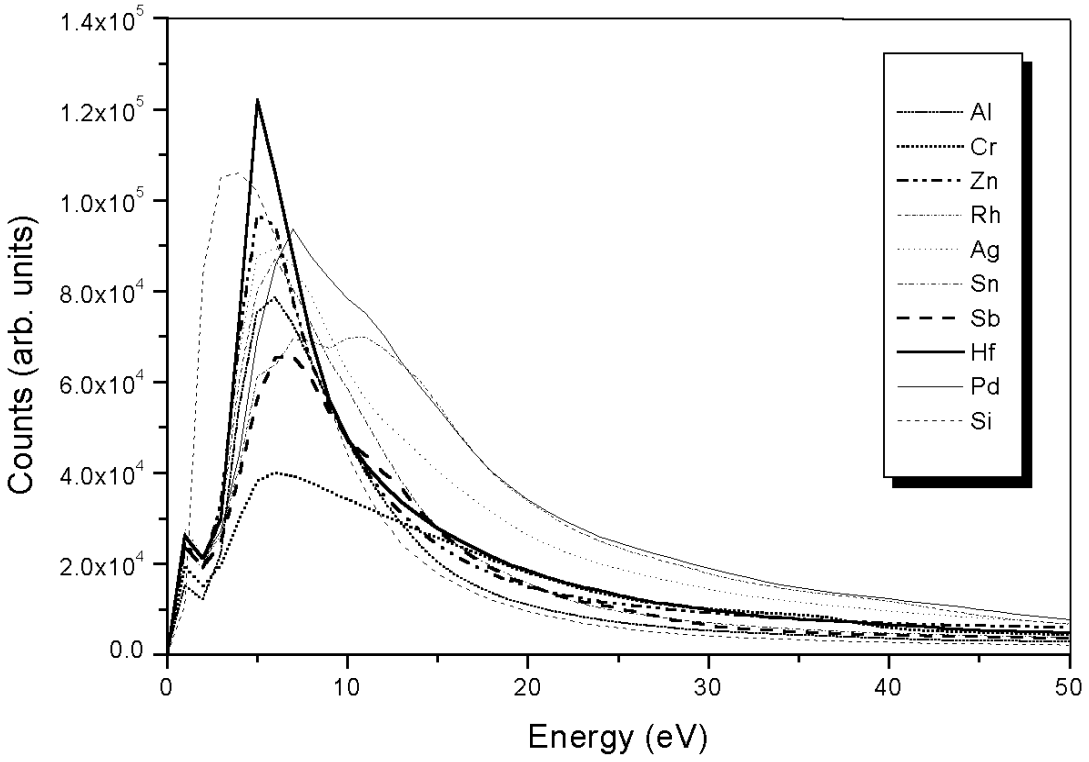

Figure 5.5. Composite plot of *N(E)* spectra from ten elements recorded at an energy of 1 keV

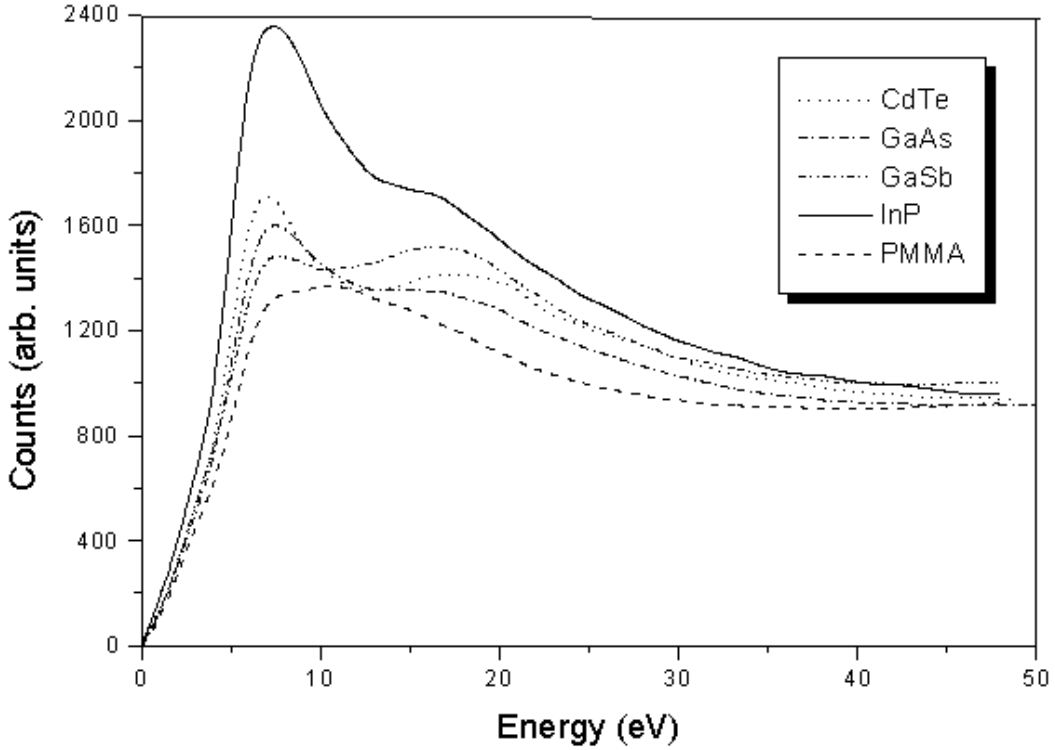

Figure 5.6(a) Composite *E.N(E)* spectra from five compound materials

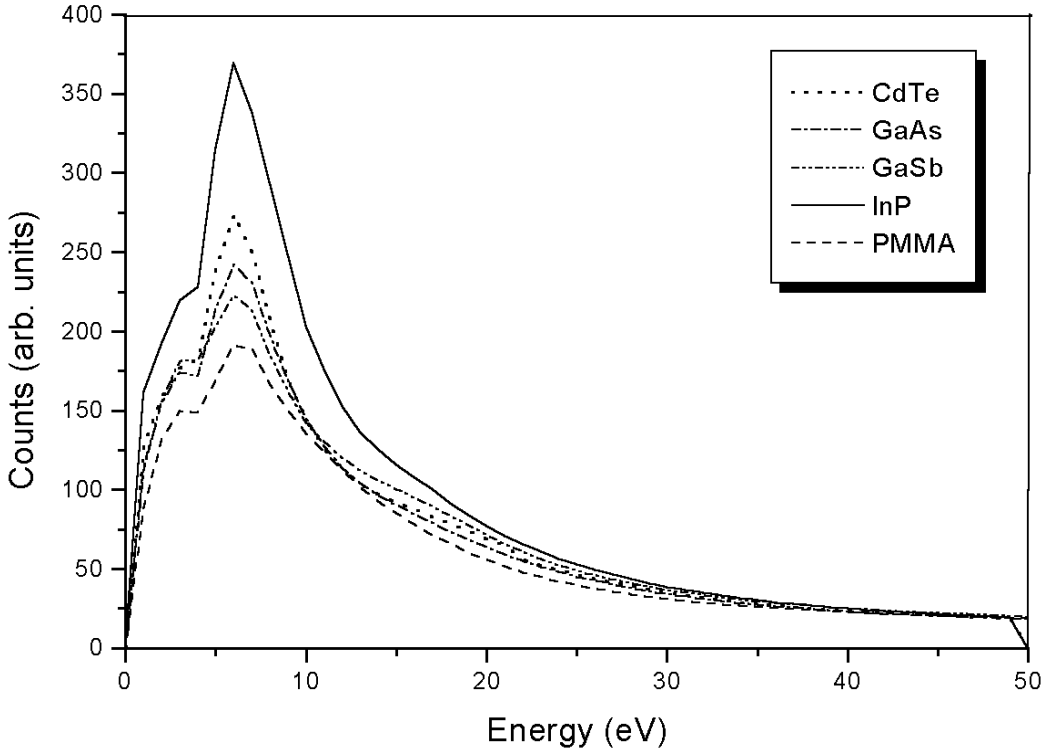

Figure 5.6(b) Composite *N(E)* spectra from five compound materials

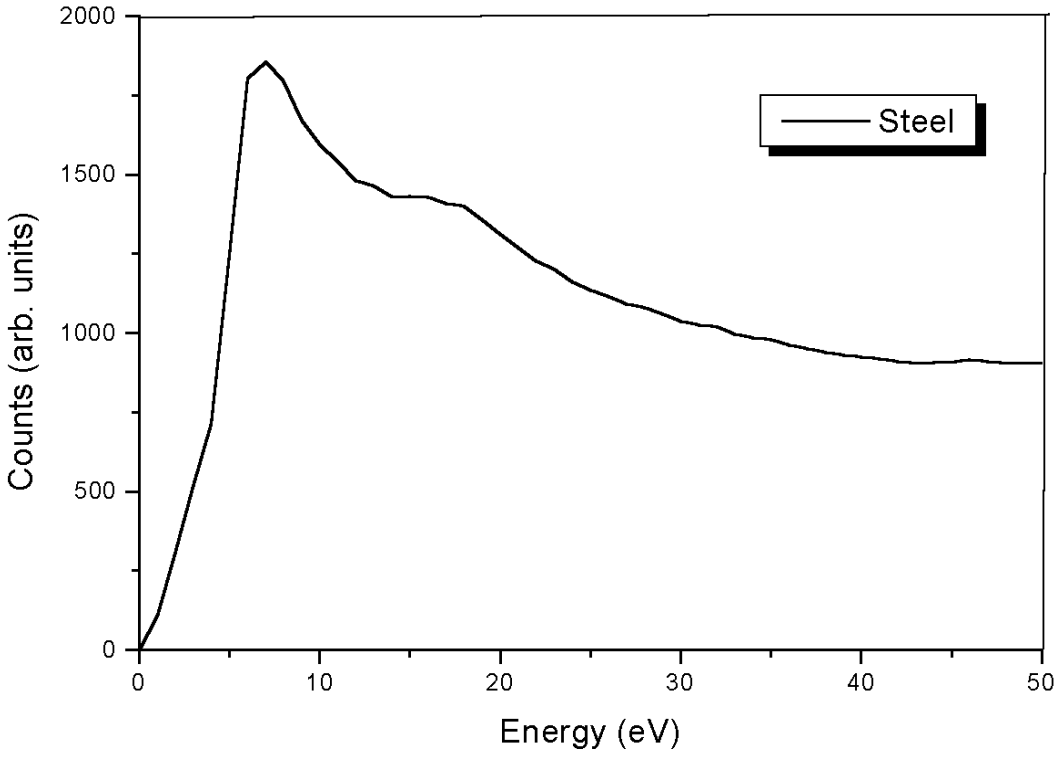

Figure 5.6(c) *E.N(E)* spectrum from a steel sample at 1 keV

shown in figure 5.2, but each contains a distinct shoulder on the high-energy side of the main peak. It is not yet possible to say definitely whether such shoulders – are which are visible in both the *E.N(E)* and the *N(E)* spectra – are always to be expected when examining a multi-element target, or whether this phenomenon is specific to the materials that were chosen for this examination. However, spectra obtained from more chemically complex materials, such as 16-6 stainless steel *E.N(E)* shown in figure 5.6(c), as well as from bronze and several other photoresist materials, do usually show evidence of a second peak, suggesting that this feature is indeed characteristic of muticomponent systems.

5.3.3 Effect of cleaning

In most cases samples were also cleaned *in situ* in the chamber after the initial measurement and then re-examined. The cleaning was performed by sputtering the sample area with a low-energy ion flood gun for a period of about 2 min. This was generally sufficient to eliminate any trace of contaminants from the spectrum as deduced from the Auger spectrum. Figure 5.7 shows the before- and after- cleaning *N(E)* spectra for Ag, Cr, Al, and lnP. For convenience the as-received and ion-sputtered spectra have been normalized to the same maximum height to facilitate comparison because the SE yield after the ion cleaning was typically 30-50% higher than that measured in the as-received condition.

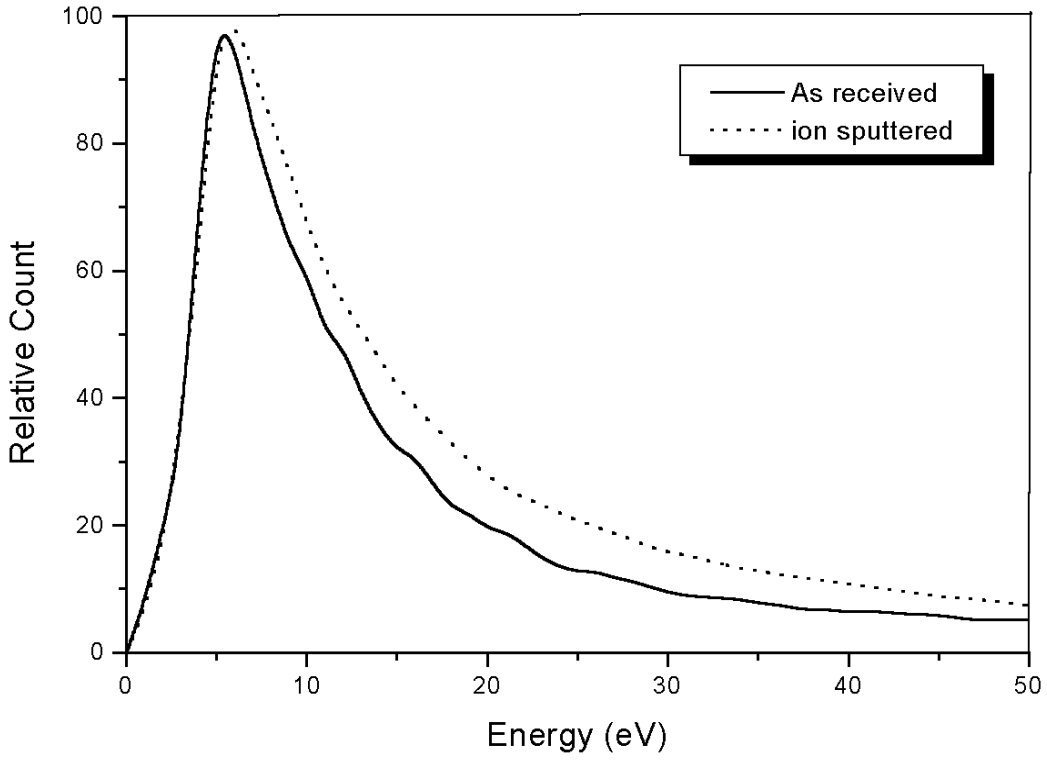

Figure 5.7(a) Comparison of *N(E)* spectra from silver in the as-received conditions and after in situ ion cleaning

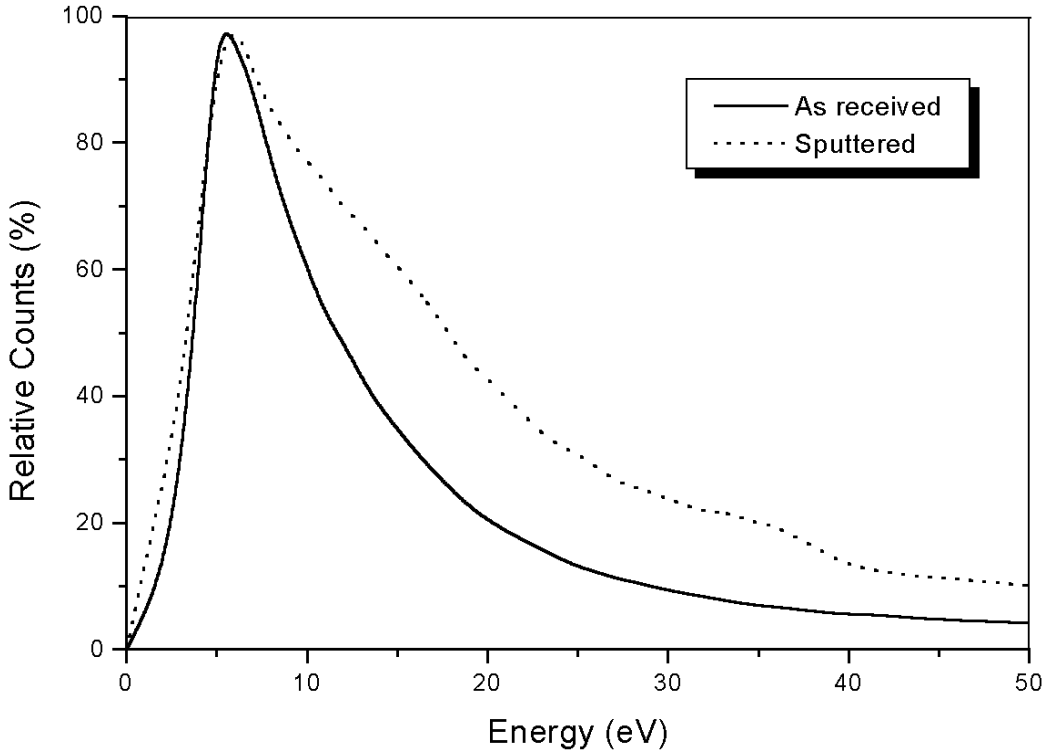

Figure 5.7(b) Comparison of *N(E)* spectra from chromium in the as-received conditions and after *in situ* ion cleaning

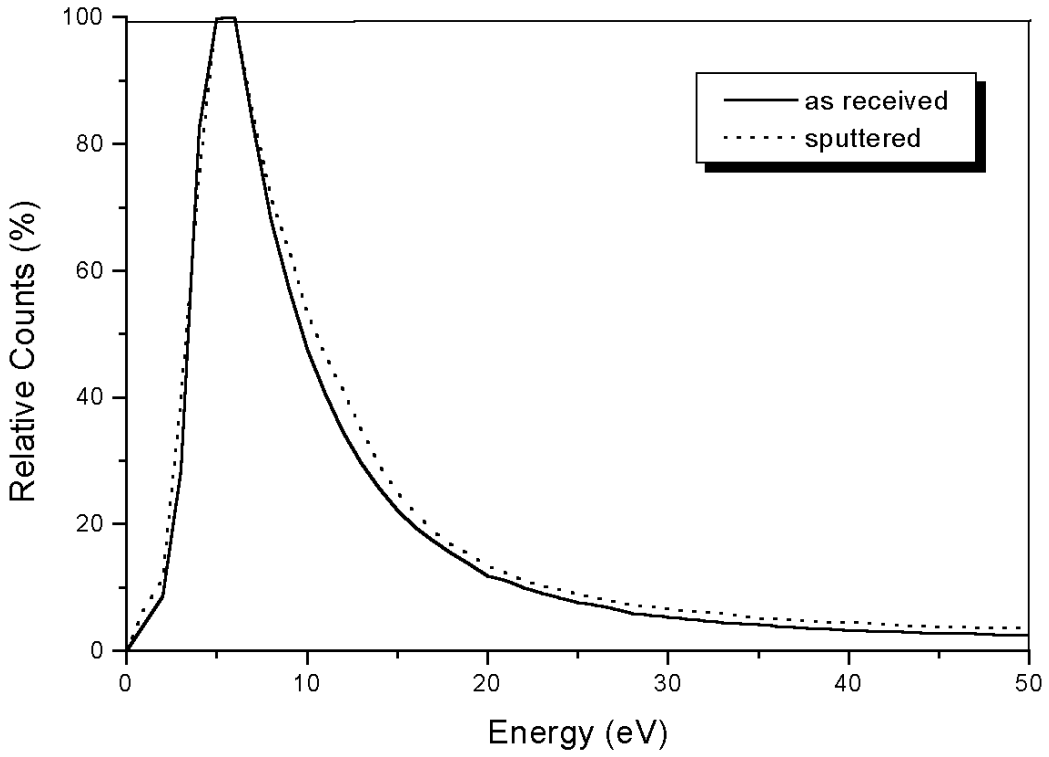

Figure 5.7(c) Comparison of *N(E)* spectra from aluminium in the as-received conditions and after *in situ* ion cleaning

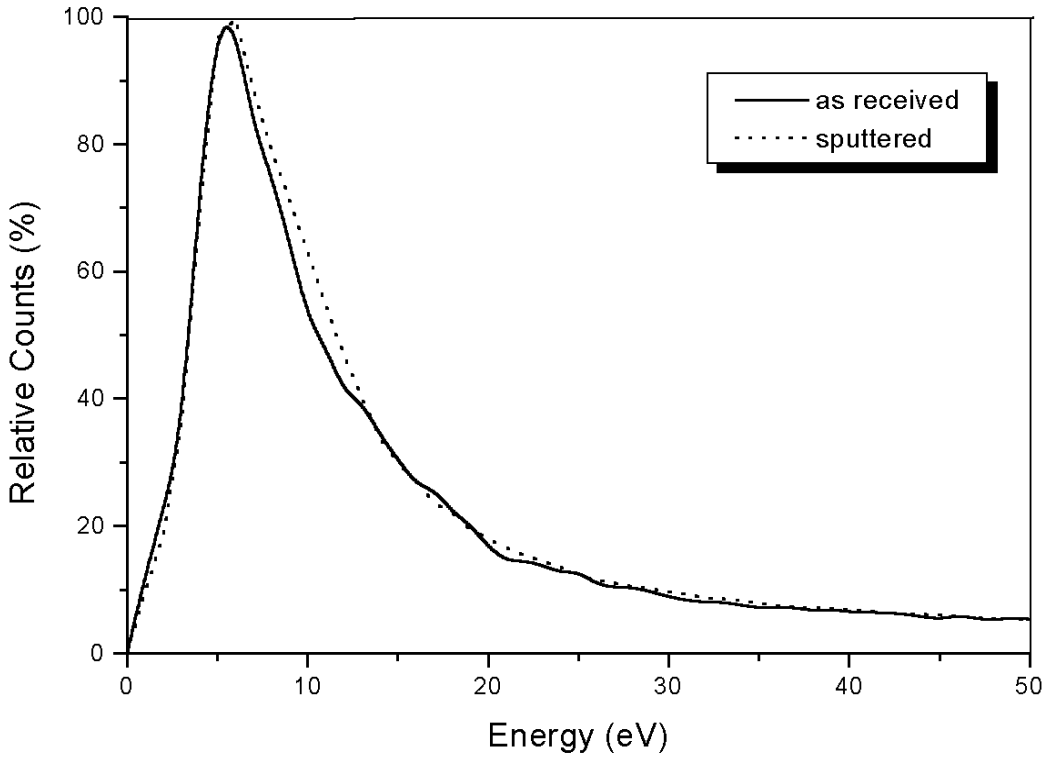

Figure 5.7(d) Comparison of *N(E)* spectra from indium phosphide in the as-received conditions and after *in situ* ion cleaning

The SE yield is reduced when the surface is dirty because the contamination layer charges positively, recollecting some of the emitted SE signal. The differences between the as-received and ion-sputtered spectra are mostly minor in nature. In each case the peak energy shifts upwards by about 1 eV after cleaning, but the width and shape of the profile remains essentially unchanged. The differences are larger in the cases of Ag and Cr than for the Al and InP samples but this may be the result of the previous history of these particular specimens or the nature of the contaminants that are present in these specific cases rather than any fundamental effect. Overall it is clear that the 'as-received' spectra are very close in form to those that can be obtained after removal of surface contaminants, implying that a large fraction of the emitted secondaries pass through these layers with only minimal disturbance.

5.4 Discussion

5.4.1 Characteristics of the spectra

The shapes of the *E.N(E)* spectra are too diverse to permit a useful description of them to be given in terms of a few simple variables. The *N(E)* spectra, however, have a sufficiently generic form that can be described in terms of a few parameters. The two most instructive have been found to be the most probable energy (Seiler, 1983)[108], i.e. the energy of the major peak in the *N(E)* spectrum, and the energy window (starting from the zero channel) within which 50% of the total emitted secondary electron signal occurs. Table 5.1 lists the values of these quantities for the 32 elements and compounds examined so far, and for 1 keV beam energy. It can be seen that the peak energy is

Table 5.1[119] Peak energy and value at which 50% of the total emitted SE signal occurs (both values in eV)

Material	50% width	Peak energy
Al	8	5
Ag	10	6
Au	11	5
C (as HOPG)	6.5	5
Cd	10	5
Co	8	5
Cr	10	4
Fe	9	5
Ge	10	5
Hf	9	5
Mo	9	5
Nb	9	5
Ni	9	5
Pb	10	5
Pt	11	5
Rh	9	5
Ru	13	11
Sb	5	11.5
Si	6.5	4
Sn	10	5
Ta	9	5
W	10	5
Zn	8	5
Zr	9	5
CdTe	9	6
GaAs	10	6
GaSb	11	6
InP	9	6
Bronze	10	6
Steel	10	6
PMMA resist	11	6
ZEP resist	18	8

typically about 5-6 eV, with the lowest being for silicon (4 eV) and the highest (11 eV) for Rh and Sb. These values are significantly higher than the 2-3 eV typically measured for clean samples under UHV conditions (Modinos, 1985)[71], from partially cleaned samples examined at UHV (Whetten & Laponsky[115]; Bleloch[112]), and from insulators examined using a low duty-cycle pulsed beam to eliminate charging (Yong & Thong, 2000)[114]. Because a thin layer of surface contamination acquires a positive charge during irradiation in the microscope the lowest energy secondaries passing through the film will be those most strongly retarded, leading to an upward shift in the apparent peak position. However, the fact that the peak energy of the samples increased still further rather than decreased after being cleaned *in situ* is anomalous. This may be evidence that ion cleaning causes surface roughening on the nanometer scale comparable with the SE escape distance. Such an effect would tend to enhance the emission of higher energy secondaries because the inelastic mean free path falls significantly as the energy is increased from 1 to 20 eV.

The energy window within which 50% of the SE signal is emitted is a measure of both the relative width of the main peak, and of the relative weighting of the lower and upper portions of the spectrum. The mean value is typically 10-11 eV, indicating the dominance of the lowest energy electrons in the signal, with a low of 5 eV for antimony and 6.5 eV for silicon and highly ordered pyrolitic graphite (HOPG), and a high of 18 eV for ZEP photoresist and 13 eV for ruthenium. The value is highest for materials, such as compound semiconductors and polymers, which are poor electrical conductors. With the

exception of antimony, which displays both the highest peak energy and the smallest 50% window width, there does not seem to be any correlation between peak and width parameters.

It is evident, from the data presented above for a wide range of materials, that the SE spectra in either their *E.N(E)* or *N(E)* format are not homogenized by the presence of surface films but display pronounced differences. Furthermore, the spectra obtained under these conditions seem to be property of the underlying material because they do not greatly vary when the contaminant layers are removed *in situ*. This is further confirmed by the reproducibility of the spectra obtained from different samples of the same material, or recorded at different times from the same specimen. This is not the same as demonstrating that these differences in some way are a characteristic expression of the chemistry of the target material rather than of the overlying contaminant surface layer. To prove this would require some indication that spectra acquired from other, similarly prepared, material but from quite independent sources show the same characteristics. Very few other SE spectra taken under 'SEM' conditions have been published, but some valuable comparative data have been given by Sakai *et.al.* (1998)[113]. Figure 5.8 compares examples of the *E.N(E)* spectra derived from the data of Sakai *et.al.* for Cu, Ag and Au with the corresponding spectra from the *in situ* cleaned samples used in this work. (Note that, although not specified as such by the authors, the Sakai *et.al.* spectra are clearly in *E.N(E)* vs. E format.) For convenience the data were normalized to the same maximum value. It can be seen that the agreement between the two is no better than suggestive for Cu, but is very close for Ag. The data for Au are very similar in form in the two examples but the spectra show a lateral offset of about 5 eV.

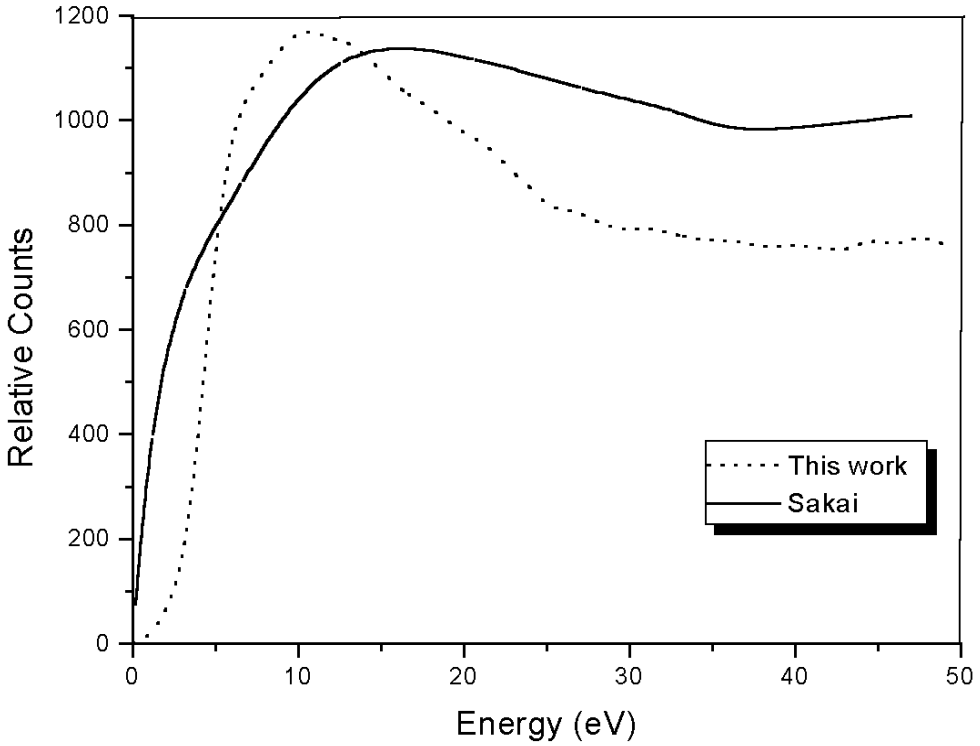

Figure 5.8(a) Comparison between *E.N(E)* spectra for copper recorded by Sakai *et.al.* (1998) and this work

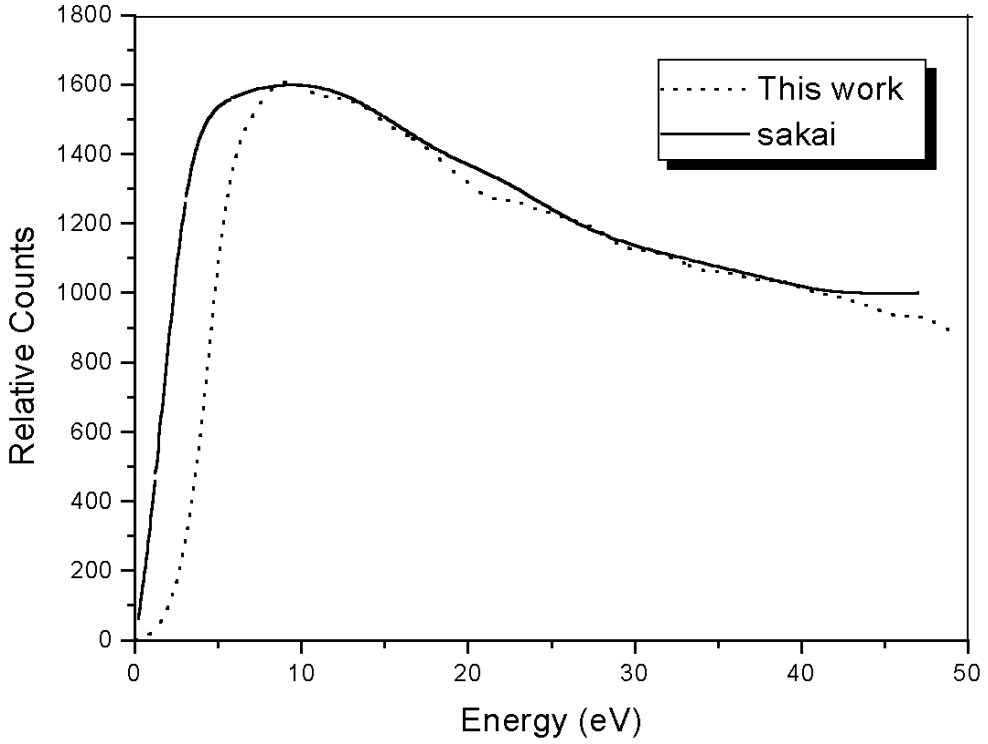

Figure 5.8(b) Comparison between *E.N(E)* spectra for silver recorded by Sakai *et.al.* (1998) and this work

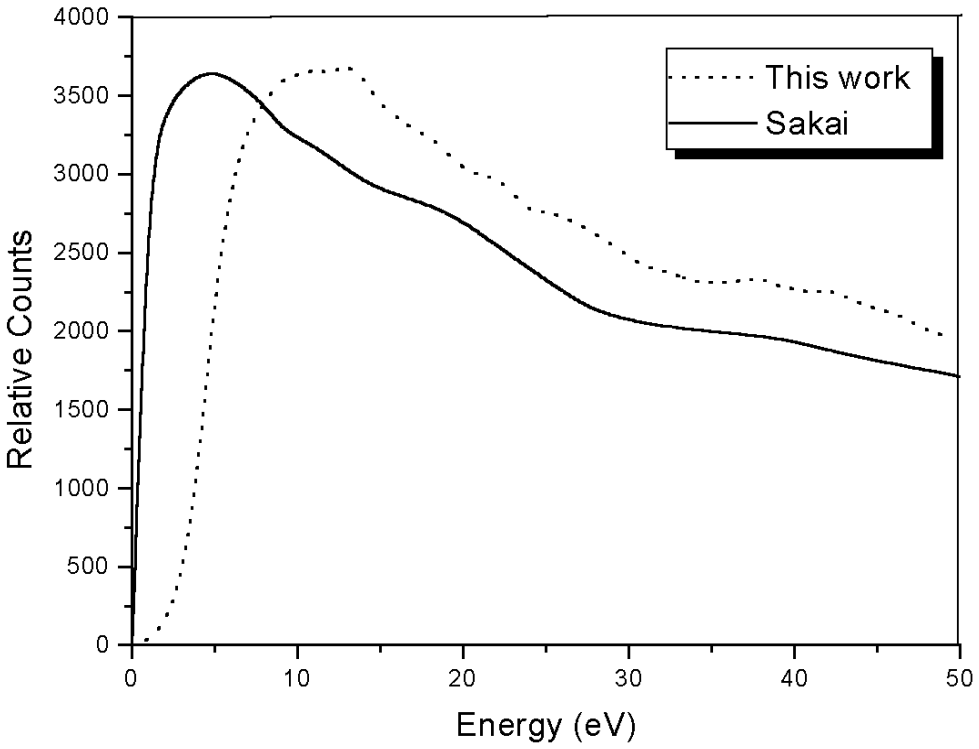

Figure 5.8(c) Comparison between *E.N(E)* spectra for gold recorded by Sakai *et.al.* (1998) and this work

(Note, however, that if these spectra are compared in the *N(E)* vs. E format these differences are minimized and visually the level of agreement is excellent in all cases.) The differences that exist between these two sets of data, and between the spectra presented here and the examples shown by other authors[112, 114, 115], can probably be attributed to environmental factors, but also to the fact that different spectrometers and collection geometries were employed in each case. The energy spectra of SE emission is different at different take-off angles from the surface because of the effects of SE transmission and reflection at the surface potential barrier[116].Thus two spectrometers collecting secondaries over a different range of angles would be expected to show somewhat different spectra. In addition the transmission efficiency of spectrometers of different design can also vary substantially over the energy range from 1 to 50 eV and this will influence the appearance of the spectrum over this wide range. In summary, this comparison with the Sakai *et.al.* spectra confirms that the SE spectra measured under the conditions used in this work are not artefactual but are properly representative of the materials examined, and that these spectra are somewhat reproducible.

5.4.2 Comparison with predicted spectra

It is also instructive to compare these experimental spectra with the theoretical models that are available. First principles calculations of SE spectra have been made (e.g. Keneko[116]; Luo & Joy[120]), but the computations required are so complex that adapting them to match the practical details of a given experimental arrangement is not practical. However, Chung & Everhart (1974)[121] have derived an expression for the total secondary electron spectrum in the form

$$\frac{dd(E)}{dE} = \frac{k}{E_{beam}} \cdot \frac{E}{(E+f)^4} \tag{5.2}$$

where d(E) is the SE yield at the emitted energy E measured with respect to the Fermi level of the sample, *k* is a normalization constant, and ? is the work function. Although this model only strictly applies to a free electron metal, the fact that the result is given in an analytical form with only one free parameter makes it a convenient template for the evaluation of spectra (Nickles *et.al.*[122]; Yong & Thong[114]). Figure 5.9(a-c) compare the *N(E)* spectra for Al, Ge and a bronze alloy, respectively, with the Chung and Everhart expression (Equation.5.2). Although there is a clear generic resemblance between the data and the model the agreement in detail is poor, even for Al, which should represent the best example for this approach. Because, from equation.5.2, the energy of the peak in the spectrum occurs at ? / 3 the analytical profile was fitted in each case by setting ? to be equal to $3E_{max}$, where E_{max} was the experimental value of the peak in the SE spectrum. Because for current data E_{max} is typically 5 eV the corresponding values of the work function ? are of the order of 15 eV, which is certainly higher than the expected value for any of these materials (see for example Kollath[73]). It should be noted that a comparison of equation 5.2 with experimental spectra from clean samples shows a better quality of fit and results in fitted values for ? that are closer to those expected (Nickles *et.al*[122].), demonstrating that the model itself does have validity.

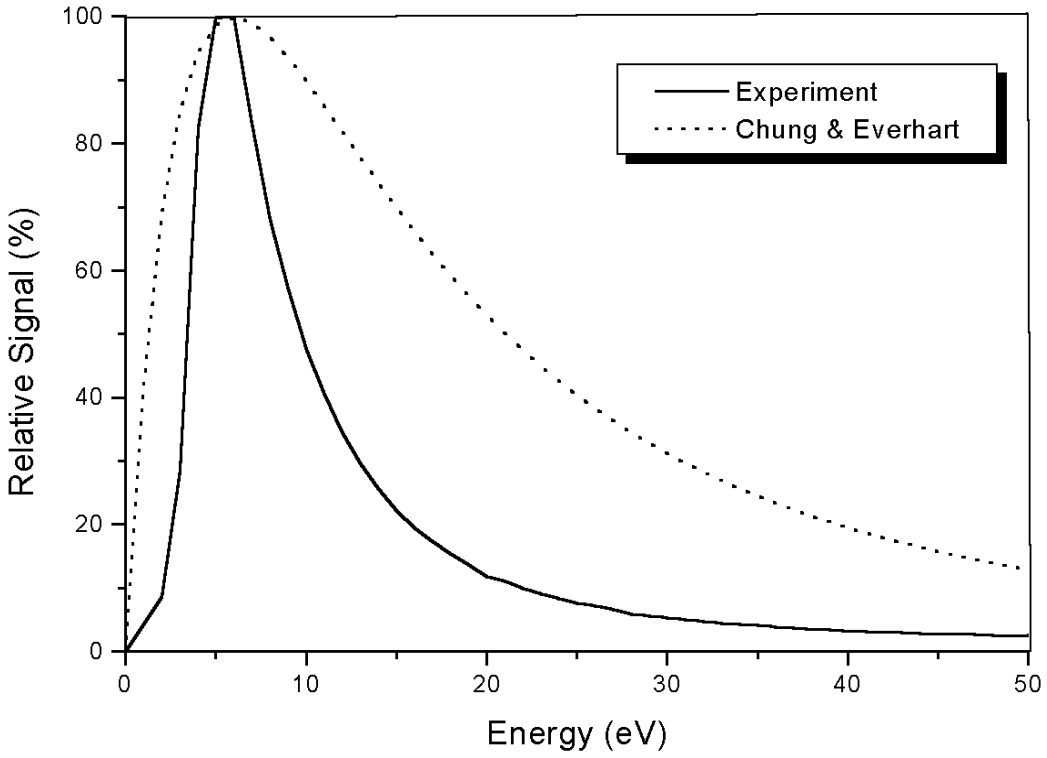

Figure 5.9(a) Comparison of experimental *N(E)* spectrum for aluminium with the Chung & Everhart (1974) model fitted to the measured peak energy

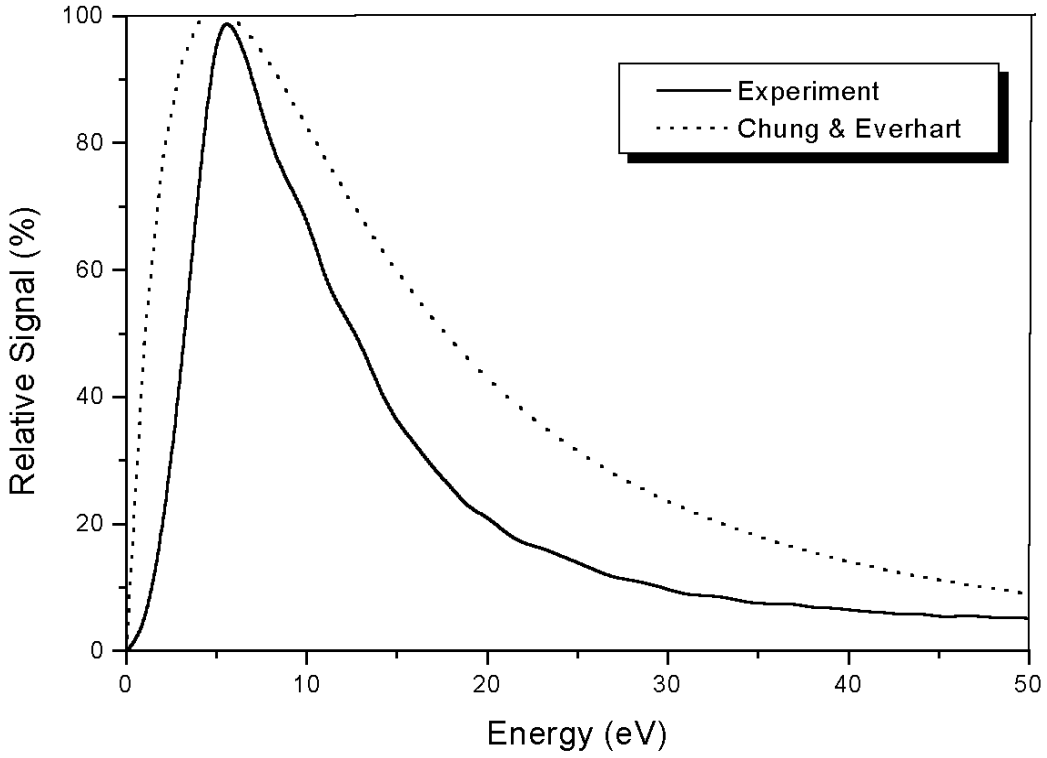

Figure 5.9(b) Comparison of experimental *N(E)* spectrum for germanium with the Chung & Everhart (1974) model fitted to the measured peak energy

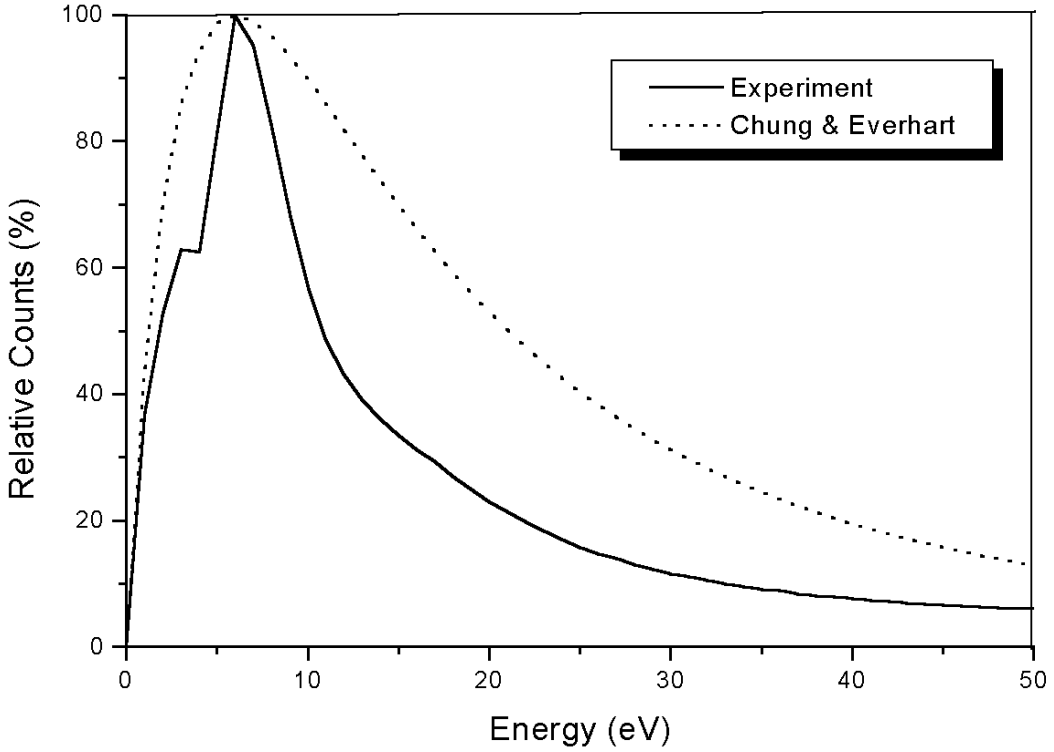

Figure 5.9(c) Comparison of experimental *N(E)* spectrum for bronze with the Chung & Everhart (1974) model fitted to the measured peak energy

5.5 Application to microanalysis

The original impetus of this study was to learn more about the nature of the SE spectrum in a typical SEM environment so that images could be interpreted more reliably and the design of detectors could be improved. However, the fact that SE spectra from different materials do show some characteristic features might suggest that SE spectroscopy could also be considered as a technique for microanalysis. The most attractive feature of such a capability would be its efficiency. Whereas the yield of fluorescent X-rays under electron irradiation is of the order of 10^{-5} photons/steradian/electron[123], the SE yield is usually in the range 0.1-1 electrons/steradian/electron. Such an enhancement would permit useful analyses to be performed in fractions of a second rather than tens of seconds. In addition, because the SE spectrum is not dependent on the incident energy, and because the SE yield increases as that energy is reduced, the technique would be ideal for use on electron beam tools that operate at low energy.

On the basis of the data shown here it is clear that it might be possible to identify pure elements from their spectra but such a capability, although interesting, is not very useful. However, it seems unlikely that the presence of individual elements in a compound could be deduced because there is no evidence that the spectrum of a compound bears any simple relationship to the spectra of its constituents. However, even given this restriction SE microanalysis could still have some utility. Figure 5.10 compares the *E.N(E)* spectra of a representative metal, semiconductor and insulator, and it can be seen that these three

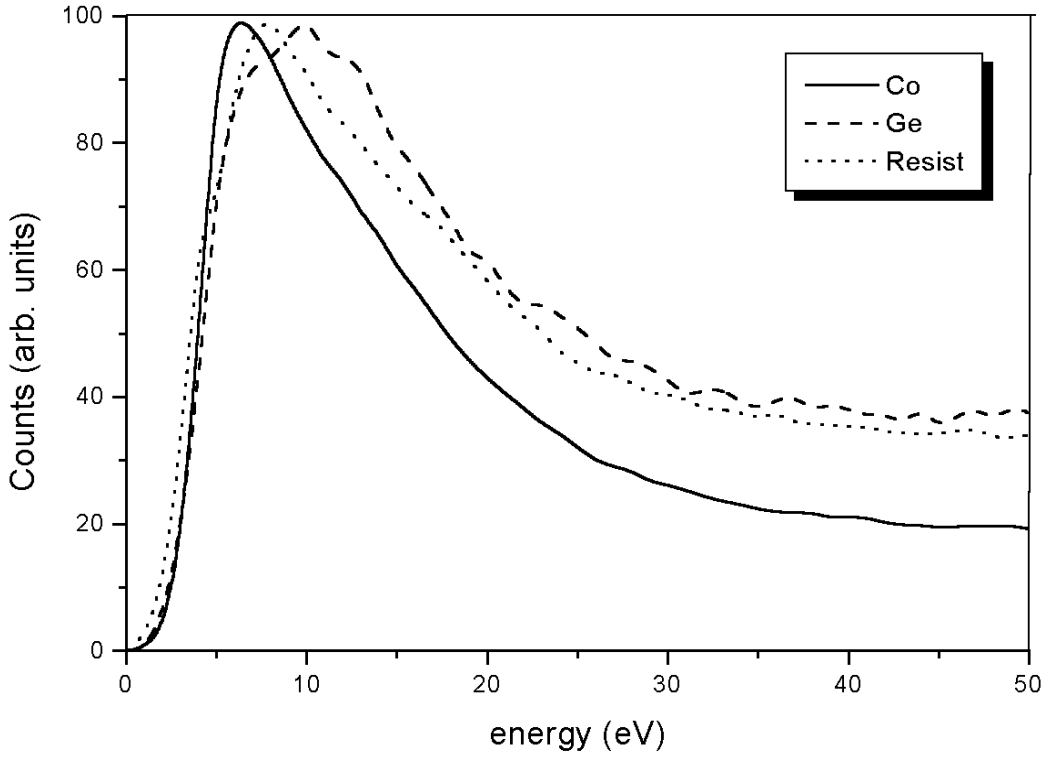

Figure 5.10 Comparison of *E.N(E)* vs. *E* spectra for a metal (cobalt), a semiconductor (germanium) and an insulator (photoresist)

types of material produce spectra with peaks of significantly different width, broad for an insulator and narrow for a metal. A comparison of spectra might therefore permit a 'triage' microanalysis, which separated materials into one of these three classes. If such an analysis could be performed in a few milliseconds it would be of value, for example, in the defect analysis of semiconductor devices. Currently 'defects' (i.e. sub micrometer-sized particles and debris on a wafer or device) are classified by their shape and size. With the use of SE spectroscopy an additional classification into metal, semiconductor and insulator could be made, which would be of great value I potentially identifying the origin of the defect. Furthermore, within a group of materials it might even be feasible to deduce the specific compound from the characteristic features of its spectrum. Figure 5.11 compares the *E.N(E)* spectra from silicon and four compound semiconductors. Although all five materials show a peak of similar width allowing them to be classed as semiconductors, each of the compound materials displays an additional shoulder and a distinctive profile. Using appropriate methods it should thus be possible to use this information to perform the next level of identification.

The use of neural networks for this purpose using the back propagation neural network package available for MathCad has been investigated [124]. After training the neural net on a library of 200 assorted spectra it is possible t perform triage with a success rate in excess of 90% on an unknown spectrum, and to identify a specific material with a success rate of about 80%. As an alternative we have also investigated the possibility of finding a compact analytical fit to experimental SE spectra so that they can be described uniquely by a small number of numerical coefficients. Spectra from unknowns could then be

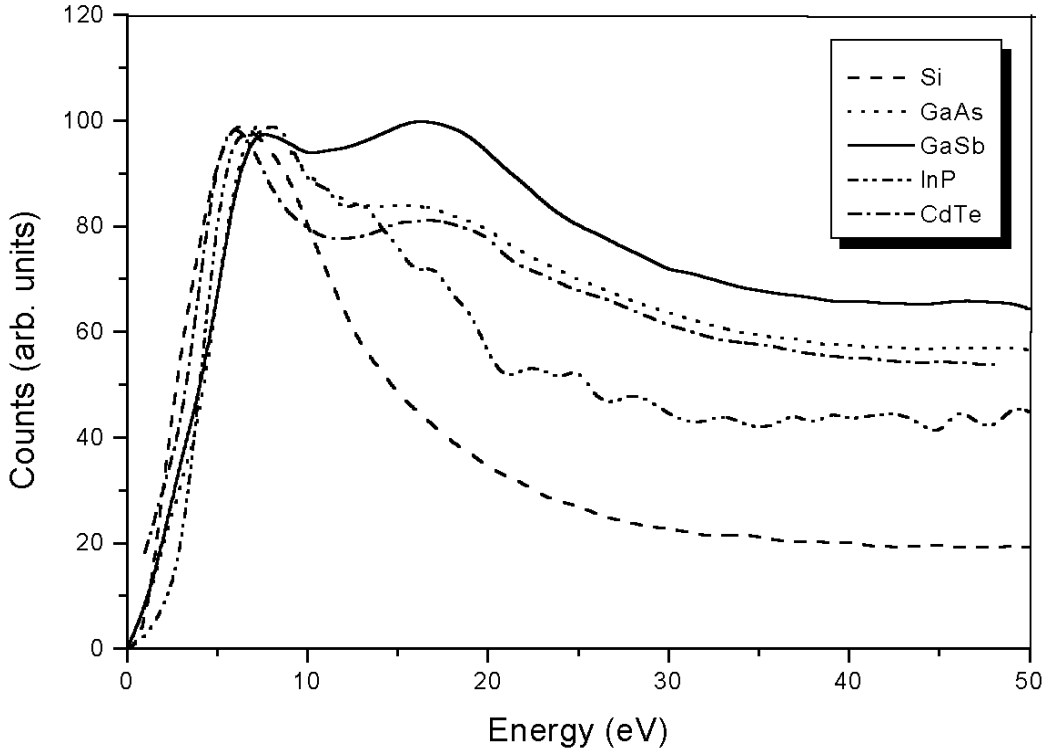

Figure 5.11. Comparison of *E.N(E)* spectra for silicon and four compound semiconductors

identified by comparing the parameters obtained from a fitted profile to those from a library of standards.

This method, which can be implemented rapidly with simple software, also shows promise and must be investigated further.

CONCLUSION

The X-ray generation efficiencies for *K*-, *L*- and *M*-lines of various elements spanning the periodic table have been experimentally determined and the parameters in the Compton & Allison equation describing these results have been determined. The functional form of the variation in the relative X-ray generation efficiency with atomic number is predicted quite well by common cross-section models and confirms their applicability to low energy microanalysis. It is shown that Compton & Allison equation is valid not only for *K*-lines but also for *L*- and *M*-lines. The monotonic variation of X-ray generation efficiency with atomic number and overvoltage can be used to estimate the unknown values from a few data sets.

Despite the presence of substantial surface contamination, the spectra from pure elements and compounds are found to be reproducible and characteristic of the underlying material when examined under conditions typical in a scanning electron microscope. These data may be of value for the design of detectors for scanning microscopy and might have applications for microanalysis.

References

1. 2001 International Technology Roadmap for Semiconductors, Semiconductor Industry Association.

2. Joy, D.C.(1998) The efficiency of X-ray production at low energies, *Journal of Microscopy*, vol.191.Pt 1, pp.74-82.

3. Castaing, R. (1951), Ph. D thesis, Univ. of Paris, Paris, France.

4. Heinrich K F.J.(1980) *Electron Beam X-ray Microanalysis*, Van Nostrand Reinhold Co., New York

5. Siegbahn, M.,(1925) *The Spectroscopy of X-Rays*, Oxford University Press, London

6. Von Hevesy, G.(1932) *Chemical Analysis by X-Rays and Its Application*, McGraw-Hill, New York

7. Goldstein, J.I., Newbury, D.E., Echlin, P., Joy, D.C., Romig, A.D., Lyman, C.E., Fiori, C. & Lifshin, E. (1992) *Scanning Electron Microscopy and Microanalysis 2nd edition*, Plenum, New York

8. Carrol Quarles , Mars Seaman (1982) *Phy Rev* A ,Volume 26

9. Clarke E (1935) A measurement of the absolute production of K-electron ionization of silver by cathode rays. Phys Rev 48:30-42

10. Joy, D.C.(1999) A database of Electron-Solid Interactions. [The complete database, containing tabulations of all available data sets as well as a comprehensive bibliography, can be downloaded as a Microsoft Word document from http://pciserver.bio.utk.edu/metrology/htm/download.shtml]

11. Joy, D.C.(2001) Fundamental constants for quantitative x-ray microanalysis, *Microscopy and Microanalysis*. 7, 159-167

12. Powell, C. J(1976) Cross-sections for ionization of inner-shell electrons by electrons. *Rev Mod Phys* 48 : 33-47

13. Campos C. S, Vasconcellos M. A. Z, Llovet X, Salvat F. (2002), Measurements of L-shell x-ray production cross-sections of W, Pt and Au by 10-30 keV electrons *Phys. Rev. A* ***66*** 012719

14. Quarles C.A, Estep L (1986) Chemical effects in K X-ray yield of sulfur. *Phys Rev* A34:2488-2492

15. Fink RW, Jopson C, Mark H, Swift CD (1966) Atomic fluorescent yields. *Rev Mod Phys* 38:513

16. Bambynek W, Crasemann B, Fink RW, Freund H-U, Mark H, Swift CD, Price RE, Rao PV (1972) Fluorescent yields for atomic excitations. *Rev Mod Phys* 44: 716-752

17. Green,M. & Cosslett, V.E. (1968) Measurements of K,L, and M shell X- ray production efficiencies. *Br. J. Appl. Phys. (J. Phys.D)* 1: 425-436

18. Lifshin, E., Ciccarelli, M.F.& Bolon,R.(1980) New Measurements of the voltage dependence of absolute X-ray yields. *Proc. 8th IXCOM, Boston 1977* (ed. By. Beaman. D.R, Ogilvie.R.E., and Wittry.D.B.), pp. 141-148. Pendell Publishers, MI

19. Bethe, H.A. (1930) Zur theorie des Durchganges schneller Korpuskalarstrahleb durch Materie. *Ann Phys* (Paris) 5: 325-349

20. ICRU (1983) Stopping Powers of Electrons and Positrons. Report #37 to the International Committee on Radiation Units. Bethesda, MD:ICRU

21. Berger, M. J, Seltzer, S. M. (1964) Studies in the Penetration of Charges Particles in Matte. Nuclear Science Series Report #39, NAS-NRC Publication 1133. Washington, DC: National Academy of Science, p 205

22. Joy, D.C., Luo, S (1989) An empirical stopping power relationship for low-energy electrons. *Scanning* 11: 176-180

23. Garber, F.W., Nakai, M.Y., Harter, J.A., Bikhoff, R.D. (1971) Low energy electron beam studies in thin aluminum foils. *J.Appl Phys* 42:1149-1158

24. Al-Ahmad, K.O., Watt, D.E. (1983) Stopping Powers and extrapolated ranges for electrons in solids. *J Phys D* 16:2257

25. Luo, S., Zhang, X., Joy, D.C. (1991) Experimental determination of electron stopping powers at low energies. *Radiat Eff Def Solids* 117:235-242

26. Joy, D.C., Luo, S., Gauvin, R., Hovington, P., Evans, N. (1996) Experimental measurements of electron stopping power at low energies. *Scannning Microscopy* 10:653-666

27. Green, M. (1962), Ph.D. Thesis, Univ. of Cambridge, Cambridge, England.

28. Green, M. and Cosslett, V.E. (1961) *Proc. Phys. Soc. London* 78, 1206

29. Worthington, C.R., and Tomlin, S.G. (1956) *Proc. Phys. Soc. A, 69A*, 401

30. Powell, C.J. (1976) in *Use of Monte Carlo Calculations in Electron Probe Microanalysis and Scanning Electron Microscopy*, Heinrich, K.F.J., Newbury, D.E., and Yakowitz, H., Eds., NBS Special Publ. 460, National Bureau of Standards, U.S. Dept. of Commerce, Washington, D.C.

31. Fabre de la Ripelle, M. (1949) *J. Phys.* (Paris) 10, 319

32. Powell, C.J (1985) Electron Impact Ionization ed Mark, T.D and Dunn, G.H (Vienna:Springer)

33. Casnati, E., Tartari, A. and Baraldi, C. (1982) *J. Phys. B: At. Mol. Phys.* 15: 155-167

34. Whiddington, R. (1911-12) *Proc. Roy. Soc., Ser. A* 86, 360; also 89, 554 (1914)

35. Duncumb, P. (1957) Ph.D. Thesis, University of Cambridge

36. Philibert, J. (1963) *Proc. 34th Intl. Symp. X-ray Optics and X-ray Microanalysis*, Stanford University (H. H. Pattee, V. E. Cosslett, and A.Engstrom, eds.) (Academic Press, New York), p. 379

37. Goldstein, J.I., Newbury, D.E., Echlin, P., Joy, D.C., Romig, A.D., Lyman, C.E., Fiori, C. & Lifshin, E. (1992) *Scanning Electron Microscopy and Microanalysis 2nd edition*, Plenum, New York **,** chapter 8 and section 9.3

38. Langenberg A., De Heer F.J., and Van Eck J. (1975) *J.Phys. B* 8, 2079

39. Hippler R., Klar H., Saeed K., McGregor I., Duncan A.J., and Kleinpoppen H. (1983) *J. Phys. B* 16, L617

40. Hippler R., McGregor I., Aydinol M., and Kleinpoppen H. (1981) *Phys. Rev. A* 23, 1730

41. Salem S.I., and Moreland L.D. (1971) *Phys. Lett. 37A*, 161

42. Davis D.V., Mistry V.D., and Quarles C.A. (1972) *Phys. Lett. 38A*, 169

43.Shima K., Nakagawa T., Umetani K., and Mikumo T. (1981) *Phys. Rev. A* 24, 72

44. Schneider H., Tobehn I., Ebel F., and Hippler R. (1993) *Phys. Rev. Lett.* 71, 2707

45. Chang C.N. (1979) *Phys. Rev. A* 19, 1930

46. Vrakking J.J., and Meyer F. (1974) *Phys. Rev. A* 9, 1932

47. Paterson J.H., Chapman J.N., Nicholson W.A.P., and Titchmarsh J.M. (1988) *J. Microscopy* 154, 1

48. Powell C.J. (1990) *Microbeam Analysis*, edited by Michael J.R. and Ingram P., (San Francisco Press, San Francisco)

49. Wisshak. F., (1930) *Ann. Phys., Lpz*., 5, 507-52

50. Braxton, W.L., Baez, A.V., and Kirkpatrik, P., (1945) *Phys. Rev*., 68, 106(abstract)

51. Kirkpatrik, P., and Baez, A.V., (1947) *Phys. Rev*., 71, 521-9

52. Dyson, N.A.(1959) *Brit. J. Appl. Phys.*, 10, 505-7

53. Dolby, R.M. (1960)) *Brit. J. Appl. Phys.*, 11, 64-6

54. Campbell, A.J. (1963) K X-ray yields from elements of low atomic number. *Proc. R. Soc. London*, A274, 319-342

55. Metchnik, V., and Tomlin, S.G. (1963), *Proc. Phys. Soc*., 81, 956-64

56. Hink, W. (1964*) Z. Phys.* 177, 424-40

57. Brown, D.B., and Ogilvie, R.E. (1964) *J. Appl. Phys*., 35, 309-14

58. Hink W. (1965*) Z. Phys.* 182, 227-37

59. http://www.oxford-instruments.com/pdf/EDSHardwareExplained.pdf

60. Fiori, C.E., Swyt, C.R. & Myklebust, R.L. (1992) DTSA – *Desk Top Spectrum Analyzer* (US Patent 529913)

61. Heinrich, K.F.J., Yakowitz, H. and Vieth, D.L. (1972) Paper 3, "*Proc. of 7th Nat. Conf. Electron Prop. Analysis*".

62. Castaing,R. & Descamps, J.(1955) Sur les bases physiques de l'analyse ponctuelle par spectrographie x.j. *Phys. Rad*. 16, 304-317

63. Joy, D.C. (1995) *Monte Carlo Modelling for Electron Microscopy and Microanalysis*, Oxford University Press, New York, 174-198

64. Jones, R.C. (1959) The statistics of electron detection. *Adv Electronics and Electron Optics 11*, 88-108.

65. Joy, D.C., Joy, C.S., Bunn, R.D. (1996) Measurement of detector efficiencies in the SEM. *Scanning*, 18, 533-538

66. http://www.cstl.nist.gov/div837/Division/outputs/DTSA/chapters/Appendix. html#A0

67. Compton, A.H. & Allison, S.K. (1935) *X-rays in Theory and Experiment*, Van Nostrand, New York

68. Drouin, D., Couture, A.R., Gauvin, R., Hovington, P., Horny, P. and Demers, H. (2000) Universite de Sherbrooke, Sherbrooke, Quebec, Canada.: *Monte Carlo simulation of electron trajectory in solids, Casino Version 2.0*

69. Austin, L and Starke, H. (1902) *Ann. Physik*, 9, 271

70. Dekker, A. J. (1958) *Secondary Electron Emission*, edited by F. Seitz and D. Turnbull, *Solid State Physics* Vol. 6 (Academic Press, New York), pp. 418.

71. Modinos, A (1985) *Field, Thermionic, and Secondary Electron Emission Spectroscopy*, Plenum Press, NewYork, pp. 327-345

72. Bruining, H.(1954) *Physics and Application of Secondary Electron Emission* (Pergamon, London)

73. Kollath, R. (1956) "Sekundarelektrnen-Emission fester Korper bei Bestrahlung mit Elektronen," *Handbuch der Physik* (Springer, Berlin), Vol.21, pp.232-303

74. Ardenne, M.von. (1956) *Tabellen der Elecktronenphysik, Ionenphysik and Ubermikoskopie* (VEB Deutscher Verlag der Wissenschaften, Berlin)

75. Jonker, J.L.H (1957) "Secondary electron emission of solids," Philips Res. Rep. 12, 249-300

76. Dekker, A.J. (1958) "Secondary electron emission," *Solid State Phys.* 6, 251-315

77. Hachenberg, O. and Bauer, W. (1959) "Secondary electron emission from solids," *Adv. Electron Phys.* 11, 413-499

78. Whetten, N.R. (1961) "A review of experimental methods in the field of secondary electron emission," General Electric Res.Lab.Rep.No. 61-RL-2733 E

79. Bronshtein, I.M. and Fraiman, B.S. (1969) *Secondary Electron Emission* (Nauka, Moscow)

80. Kanter, H (1961) "Contribution of backscattered electrons to secondary electron formation," *Phys.Rev.* 121, 681-684

81. Jahrreiss, H. (1965) "Uber einige Erweiterungsmoglichkeiten der Sternglass'schen Theorie der Sekundarelektronen Emission," *Ann. Phys.* (VII) 14, 325-352

82. Wittry, D.B (1966) "Secondary electron emission in the electron probe," *Optique de rayon X et microanalyse*, edited by Castaing, Descamps, and Philibert (Herrman, Paris), pp. 168-188

83. Mayer, H., and Holzl, J. (1966) "Experimentelle Bestimmung der maximalen Austrittstiefen monoenergetischer Sekundarelektromen," *Phys. Status Solidi* 18, 779-785

84. Seiler, H (1967) "Some problems of secondary electron emission," *Z. Angew Phys.* 22, 249-263

85. Seiler, H (1968) "Die physikalischen Aspekte der Sekundarelektronen emission fur die Elecktronen-Raster-Mikroskopie," Beitrage Elektr. Direktabb. Oberflachen (BEDO) (edited by G.Pfefferkorn)1, 27-52

86. Applet, G (1968) "Fine structure measurements in the energy angular distribution of secondary electrons from a (110) face of copper," *Phys. Status Solidi* 27, 657-669

87. Simon, R.E. and Williams, B.F (1968) "secondary electron emission," *J. IEEE Trans. Nucl. Sci.* NS-15, 167

88. Seah, M. P (1969) "Slow electron scattering from metals," *Surf. Sci.* 17, 132-213

89. Drescher, H., Reimer, L., and Seidel, H. (1970) "Ruckstreukoeffizient and Sekundarelektronen- Ausbeute von 10-100 keV-Elektronen und Beziehungen zur Raster-Elecktronenmikroskopie," *Z. Angew. Phys.* 29, 331-336

90. Shimizu, R. and Murata, K. (1971) "Monte-Carlo calculations of the electron-sample interactions in the scanning electron microscope," *J. Appl. Phys*. 42, 387-394

91. Kanaya, K. and Kawakatsu, H. (1972) "Secondary electron emission due to primary and backscattered electrons," *J. Phys. D* 5, 1727-1742

92. Murata, K. (1973) "Monte-Carlo calculations on electron scattering and secondary electron production in the SEM," *Proc. SEM Conf*., edited by O.Johari, Vol.2, pp.267-276

93. Shimizu, R. (1974) "Secondary electron yield with primary electron beam of kilo-electron-volts," *J. Appl. Phys.* 45, 2107-2111

94. Fitting, H. J. (1974) "Transmission, energy distribution and secondary electron excitation of fast electrons in thin solid films," *Phys. Status Solidi A* 26, 525-535

95. Fitting, H. J. (1980) "Some aspects of electron emission from solids," *Exp. Tech. Phys.* 28, 321-329

96. Willis, R. F., and Feuerbach, B. (1975) "Angular-resolved secondary electron emission spectroscopy of clean and adsorbate covered tungsten single crystal surfaces," *Surf. Sci.* 53, 144-155

97. Voreades, D. (1976) "Secondary electron emission from thin carbon films," *Surf. Sci.* 60, 325-348

98. Pillon, J., Roptin, D., and Cailler, M. (1976) "Secondary electron emission from aluminum," *Surf. Sci.* 59, 741-748

99. Chung, M.S. and Everhart, T.E. (1977) "Role of plasmon decay in secondary electron emission in the nearly free electron metals-application to aluminum," *Phys. Rev. B* 15, 4699-4715

100. Reimer, L. and Drescher, H. (1977) "Secondary electron emission of 10-100 keV electrons from transparent films of Al and Au," *J. Phys. D* 10, 805-815

101. Kanaya, K. and Ono, S. (1978) "The energy dependence of a diffusion model for an electron probe into solid targets, *J. Phys. D* 11, 1495-1508

102. Alig, R.C. and Bloom, S. (1978) "Secondary electron escape probabilities," *J. Appl. Phys.* 49, 3476-3480

103. Ono, S. and Kanaya, K. (1979) "The energy dependence of secondary emission based on the range-energy retardation power formula," *J. Phys. D* 12, 619-632

104. Ganachaud, J. P. and Cailler, M. (1979) "A Monte Carlo calculation of the secondary electron emission of normal metals," *Surf. Sci.* 83, 498-530

105. Chase, R. E., Gordon, W. L., and Hoffman, R. W (1980) "Measurement of low energy secondary electron distribution using a double-pass cylindrical mirror analyzer," *Appl. Surf. Sci.* 4, 271-281

106. Rosler, M. and Brauer, W (1981) "Theory of secondary electron emission," *Phys. Status Solidi B* 104, 161-175, 575-587

107. Cailler, M., Ganachaud, J. P., and Bourdin, J. P (1981) "The mean free path of an electron path of an electron in copper between two inelastic collisions," *Thin Solid Films* 75, 181-189

108. Seiler, H (1983) "Secondary electron emission in the scanning electron microscope," *J. Appl. Phys*. 54 (11), R1-R18

109. Halbritter, J. (1982) "On conditioning: Reduction of secondary- and rf-field emission by electron, photon, or helium impact," *J. Appl. Phys.* 53, 6475-6478

110. Joy, D. C. & Joy, C. S. (1999) Study of the dependence of E_2 energies on sample chemistry. *Microsc. Microanal*. 4, 475-481

111. Joy, D. C. (2003) For an annotated compilation of experimental secondary electron yield data see http://pciserver.bio.utk.edu/metrology

112. Bleloch, A. L. (1989) SE spectroscopy and image resolution in a STEM. *Inst. Phys. Conf. Series*, 98, 469-472

113. Sakai, Y., Yamada, T., Suzuki, T., Sato, T., Itoh, H. & Ichinokawa, T. (1998) Contrast mechanisms in scanning ion microscope. *Appl. Phys. Lett*. 73, 611-613

114. Yong, Y. C. & Thong, J. T. L. (2000) Determination of SE spectra from insulators. *Scanning*, 22, 161-166

115. Whetten, N. R. & Laponsky, A. B. (1957) Energy distribution of secondary electrons from MgO single crystals. *Phys. Rev*. 107, 1521-1524

116. Keneko, T. (1990) Energy distribution of secondary electrons. *Surf. Sci*. 237, 327-336

117. Grais, K. I. & Bastawros, A. M (1982) A study of secondary electron emission in insulators and semiconductors. *J. Appl. Phys*. 53, 5239-5242

118. Oechsner, H. (1993) Recent instrumental developments in surface and thin-film analysis by electron and mass spectrometric techniques. *App. Surf. Sci.* 70/71, 250-260

119. Joy, D. C., Satya P. M., and Meyer III, H. M (2004) "Experimental Secondary Electron Spectra under SEM conditions" *Journal of Microscopy,* Vol.215 (1), p77, 9p

120. Luo, S. & Joy, D. C. (1990) Monte Carlo calculations of secondary electron emission. *Scanning electron Microsc. Suppl.* 4, 127-146

121. Chung, M. S. & Everhart, T. E (1974) Simple calculation of energy distribution of low-energy SE from metals. *J. Appl. Phys.* 45, 707-709

122. Nickles, N., Davis, R. E. & Dennison, J. R. (2000) Applications of SE energy and angular distributions to spacecraft charging. *6th Spacecraft Charging Technology Conference,* AFRL-VS-TR-20001578, pp. 275-280

123. Prasad, M. S. & Joy, D. C. (2003) Measurements of absolute X-ray generation efficiency for selected K, L, and M- lines. *Scanning*, 25, 210-215

124. Neeraj Khanna (1999) *Secondary Electron Spectroscopy*, Thesis**,** University of Tennessee, Knoxville, U.S.A

VITA

Satya Mulapudi was born in Rajahmundry, India on October 6, 1975. After completing high school from Siddhartha junior college, India, in 1993, he entered Metallurgical Engineering department at the Regional Institute of Technology, Jamshedpur, India which is affiliated to Ranchi University. Upon graduation with distinction in 1997, he joined Tata Motors Ltd as a production engineer.

In fall of 2000 he was admitted to the Materials Science and Engineering department at the University of Tennessee, Knoxville as a prospective PhD candidate under the guidance of Dr. David C. Joy. Since then he has been working on the fundamental studies of X-ray and Secondary Electron Spectroscopy. In summer 2003, he interned with Procter and Gamble in Cincinnati, Ohio, working on low voltage X-ray microanalysis. His research was recognized in 2002 with the Microbeam Analysis Society Distinguished Scholar award. Satya Mulapudi has published research papers in Scanning and Journal of Microscopy as well as contributed posters to several conferences.